Developmental Defects in Huntington's Disease Show That Axonal Growth and Microtubule Reorganization Require NUMA1

Mariacristina Capizzi, Rémi Carpentier, Eric Denarier, Annie Adrait, Rayane Kassem, Marina Mapelli, Yohann Couté, Sandrine Humbert

Developmental Defects in Huntington Disease Show that Axonal Growth and Microtubule Reorganization Require NUMA1

Mariacristina Capizzi[1], Rémi Carpentier[1], Eric Denarier[1], Annie Adrait[2], Rayane Kassem[1], Marina Mapelli[3], Yohann Couté[2] and Sandrine Humbert[1]

[1]Univ. Grenoble Alpes, Inserm, U1216, CEA, Grenoble Institute Neurosciences, 38000 Grenoble, France

[2]Univ. Grenoble Alpes, Inserm UMR BioSanté, U1292, CNRS, CEA, FR2048, 38000 Grenoble, France

[3]IEO, European Institute of Oncology IRCCS, Via Adamello 16, 20139 Milan, Italy

*Correspondence and Lead Contact:
Sandrine Humbert
Grenoble Institut des Neurosciences, Inserm U1216, UGA
Bâtiment Edmond J. Safra
Chemin Fortuné Ferrini
38700 La Tronche, France
Phone: +33 (0)4 56 52 06 29
Email: sandrine.humbert@univ-grenoble-alpes.fr

SUMMARY

Although the classic symptoms of Huntington's disease (HD) manifest in adulthood, neural progenitor cell behavior is already abnormal by thirteen weeks' gestation. To determine how these developmental defects evolve, we turned to cell and mouse models. We found that layer II/III neurons that normally connect the hemispheres are limited in their growth in HD by microtubule bundling defects within the axonal growth cone, so that fewer axons cross the corpus callosum. Proteomic analyses of the growth cones revealed that NUMA1 (Nuclear/Mitotic Apparatus protein 1) is downregulated in HD by miR-124. Suppressing NUMA1 in wild-type cells recapitulates the microtubule and axonal growth defects of HD, whereas raising NUMA1 levels with antagomiR-124 or stabilizing microtubules with epothilone B restore microtubule organization and rescues axonal growth. NUMA1 therefore regulates the microtubule network in the growth cone, and HD, which is traditionally conceived as a disease of intracellular trafficking, also disturbs the cytoskeletal network.

Keywords: Huntington disease, neurodevelopment, axonal growth, microtubule bundling, Nuclear Mitotic Apparatus protein 1 (NUMA1)

INTRODUCTION

Huntington disease (HD) is caused by an abnormal CAG expansion in the coding region of the *huntingtin* gene, which leads to the production of huntingtin protein (HTT) that bears an abnormally long polyglutamine tract. The classic motor and cognitive symptoms of HD do not typically appear until adulthood but neuroimaging studies have revealed clear abnormalities in brain structure and function in presymptomatic mutation carriers (Nopoulos et al., 2011; Scahill et al., 2020; Tang et al., 2013; Tereshchenko et al., 2020). Although such changes may be a mix of compensatory, degenerative, and developmental processes, one recent study in HD subjects deduced that their lack of asymmetry between the right and left Sylvian fissure (which should be formed around the fourteenth gestational week) must arise during embryogenesis (Mangin et al., 2020). This was the most suggestive evidence for very early developmental derangement in humans until we were able to study fetal HD mutation carrier tissue and demonstrate molecular abnormalities in neural progenitor cells (Barnat et al., 2020). Because there are so few human samples available, however, and we were limited to studying tissue from 13-week-old fetuses, we were unable to follow the evolution of these molecular defects.

The literature provides a number of hints as to where we should look. HD is most prominently associated with degeneration of the corticostriatal circuit, which may have as much to do with modification of wild-type HTT function as with dysfunction of the mutant HTT (mHTT). During cortical development, projection neurons produced in the ventricular zone undergo a multipolar-bipolar transition and migrate along the glial fibers to reach their designated layer in the cortical plate, where they integrate and mature. The HTT protein normally maintains the pool of cycling neural progenitors and ensures the multipolar-bipolar transition of newborn neurons and their proper migration (Barnat et al., 2017; Godin et al., 2010). In HD mice, mHTT causes mitotic spindle misorientation of dividing progenitors and decreases cortical thickness at E14.5 and E16.5 (Molina-Calavita et al., 2014). mHTT also interferes with the migration and maturation of post-mitotic neurons (Barnat *et al.*, 2017; Cepeda et al., 2003; McKinstry et al., 2014; Molero et al., 2016). Our study of human HD mutation carrier fetuses (Barnat *et al.*, 2020) showed that, as in HD mouse models, the number of proliferating cells is diminished, and more neural progenitors enter lineage specification prematurely. To this subtle defect in neurogenesis we can add defects in neural migration, as some layer-specific neocortical neurons mislocalize in the mouse (Barnat *et al.*, 2017). It is not

known whether the neurons are able to integrate properly into the circuit once they reach their destination. We therefore asked whether HD affects axonal growth.

Axonal growth takes place through the growth cone, a highly motile structure located at the tip of the growing axon (reviewed in (Lewis et al., 2013; McCormick and Gupton, 2020; Pasterkamp and Burk, 2020; Pinto-Costa and Sousa, 2021)). The growth cone receives guidance cues from the extracellular environment and remodels the cytoskeleton accordingly to enable axonal outgrowth. This cytoskeletal reorganization inside the growth cone generates two opposing forces: a "push" from the axonal shaft, driven by microtubule polymerization, and a "pull" from the retrograde flow of ACTIN at the front of the growth cone. Studies in cell models examining how neuritic outgrowth might be affected in HD have yielded somewhat inconsistent results: one study reported longer neurites in neural cultures derived from HD patient-derived induced pluripotent stem cells (iPSC) (Consortium, 2017), but other studies show shorter neurites in neural cultures derived from HD iPSCs (Mehta et al., 2018), in primary cultures of hippocampal neurons expressing the first exon of mHTT (Ilieva et al., 2019) and in HD neuroblastoma cell lines (Reis et al., 2011). Multiple neuroimaging studies, however, clearly show that the corpus callosum, which integrates function across the hemispheres, is thinner in HD gene carriers (reviewed in (Casella et al., 2020; Estevez-Fraga et al., 2020)). In HD mice, as in humans, diffusion imaging reveals thinning of the white matter tracts of the corpus callosum (reviewed in (Casella *et al.*, 2020)). This thinning has been attributed to the degeneration of callosal axons and myelination deficiencies, but given the early developmental defects in HD, we hypothesized that it actually reflects abnormal axonal growth.

RESULTS

Axonal growth of callosal projection neurons is attenuated in HD from P0

To analyze the axonal growth of callosal neurons in HD, we studied an HD knock-in mouse model in which the first exon of the HTT gene is replaced by a human exon 1 carrying 111 CAG repeats ($Hdh^{Q7/Q111}$)(Wheeler et al., 2002). $Hdh^{Q7/Q111}$ heterozygous mice express mHTT at the endogenous level, recapitulate the genetics of human HD, and provide a reliable model of neurodevelopmental processes that take place in HD human embryos (Barnat *et al.*, 2020).

Callosal projection neurons originating from pyramidal neurons of the superficial cortical layers II/III connect homotopically to the contralateral cortex (Fame et al., 2011). We performed in utero electroporation (IUE) of the membrane-targeted red fluorescent protein (mem-RFP) in the somatosensory cortex of mouse embryos at embryonic day 15.5 (E15.5), when the neurons that form layers II and III are born (Figure 1A) (Hand et al., 2015). We then measured axonal length at post-natal day 0 (P0), when fibers begin to cross the corpus callosum (Figures 1A and B, upper panel). Axons were shorter in $Hdh^{Q7/Q111}$ embryos than in their $Hdh^{Q7/Q7}$ controls and remained so even at P4 (Figure 1B, lower panel). Another HD mouse model, zQ175, showed the same axonal growth defect (Figure S1A) (Menalled et al., 2012).

We next analyzed neuronal development at P21, when the axons have reached their final destination and are connected to the contralateral side. As before, we electroporated mem-RFP in the somatosensory cortex of E15.5 mouse embryos and selected four regions of interest (Figure 1C). Previous studies reported that layer II/III neurons form branches both ipsi- and contra-laterally in layers I/II/III and V, but not in layer IV (see e.g. (Hand *et al.*, 2015; Lewis *et al.*, 2013)). We made the same observation in P21 axons of $Hdh^{Q7/Q7}$ mice (Figures S1B and S1C). To assess ipsilateral arborization (region 1, somatosensory cortex), we calculated the signal intensity in layer V (Figure S1B); this signal was similar in $Hdh^{Q7/Q7}$ and $Hdh^{Q7/Q111}$ animals. For the contralateral region, we chose region 2, within the area corresponding to the somatosensory cortex, where branching reached its maximum density for both genotypes (Figures 1C and S1C). Signal intensities were lower in $Hdh^{Q7/Q111}$ layers II/III and V than in $Hdh^{Q7/Q7}$ animals (Figure S1C).

To determine whether the sparser arborization in the contralateral region was due to fewer axons arising from the ipsilateral side, we measured the signal intensity in the white matter (WM) region of region 2 and found it to be lower in the $Hdh^{Q7/Q111}$ animals, i.e., they had fewer axons than controls (Figure S1C). We next traced the axons along the corpus callosum (Figure 1C, region 3) and measured signal intensity along the line with a fixed width of 200 pixels. Axonal density in the $Hdh^{Q7/Q111}$ corpus callosum was lower than in $Hdh^{Q7/Q7}$ controls (Figure 1D). To measure the contralateral arborization relative to the number of axons that actually reached the contralateral side, we evaluated the signal intensity in layers V and II/III relative to the white matter (Figure S1C, bottom graphs). Here the HD mice showed greater arborization, which likely reflects compensation for the lower number of axons.

Lastly, we analyzed the pattern of branching along the regions of the cortex from the corpus callosum to the contralateral region (Figure 1E). We drew a line coronally, focusing on layer II/III, where the axons end (Figure 1C, region 4). In control sections, there were several branching points in the parietal (Figure 1E, areas a and b) and somatosensory regions (Figure 1E, areas c and d). In HD, the major branching area was in the somatosensory cortex. In agreement with our previous quantification (Figure S1C), branching was less dense in HD than in control brains.

Thus, neonatal axonal growth limitation in HD still affects branching in the contralateral cortex at P21.

Microtubule disorganization leads to HD cortical neuron growth cone defects

To investigate the morphology of callosal axons at a single-cell resolution, we established a cellular model of layer II/III neurons. We developed primary cultures of wild-type ($Hdh^{Q7/Q7}$) cortical neurons from E16.5 embryonic mouse brains electroporated at E15.5 with a plasmid encoding myristoylated-Venus (mVenus), a variant of the yellow fluorescent protein (Figure 2A). At four Days In Vitro (DIV4), we identified mVenus-positive cells by staining against the cortical layer markers Satb2 and Ctip2, which are expressed in callosal projection and layer V neurons, respectively (Alcamo et al., 2008). Most of the mVenus-positive neurons were Satb2-positive and Ctip2-negative. We developed cultured cells from $Hdh^{Q7/Q7}$ and $Hdh^{Q7/Q111}$ embryos using the same cell culture conditions and measured the axonal length of mVenus-positive cells. Axons were shorter in HD than in wild-type cultured neurons (Figure 2B), mimicking the in vivo condition (Figure 1). Axonal branching, however, was similar in control and HD neurons at this developmental stage in vitro (Figure 2B).

Since a decrease in neuritic growth correlates with an increase in growth cone size (Ren and Suter, 2016), we labeled the F-ACTIN network with phalloidin to delineate the growth cone periphery and to compare the growth cone area in control and HD neurons. As expected from the inhibited axonal growth in HD, the growth cone area in cortical $Hdh^{Q7/Q111}$ neurons was significantly larger than in $Hdh^{Q7/Q7}$ neurons (Figure 2C). The growth cone owes much of its morphology and directional motility to the dynamic reorganization of microtubules. In the shaft of the axon, microtubules are bundled together, but upon entering the growth cone they splay out into individual "exploratory microtubules" that extend into the distal, motile domain and invade

the ACTIN cytoskeleton (Dent et al., 2011). To examine the microtubules, we used an anti-tyrosinated TUBULIN antibody that reveals both the main microtubule bundle and the exploratory microtubules (Figure 2D). This tyrosinated TUBULIN signal was significantly lower in HD growth cones, indicating abnormally bundled microtubules (Figure 2D). This was confirmed by the lower mean maximum fluorescence intensities in HD compared to control neurons (Figure 2D, blue and orange arrows on linescan correspond to the bundles in control and HD growth cones, respectively). The exploratory microtubules in the peripheral domain were also longer in $Hdh^{Q7/Q111}$ than in $Hdh^{Q7/Q7}$ neurons, in agreement with the loose bundling in HD. We conclude that HD defective axonal growth is associated with microtubule disorganization in the growth cones.

HD alters the protein composition of growth cones

To decipher the molecular basis of HD-induced defects in axonal growth in an unbiased manner, we performed mass spectrometry (MS)-based quantitative proteomic analysis on control and HD growth cones prepared from cortices of newborn $Hdh^{Q7/Q7}$ and $Hdh^{Q7/Q111}$ mice using sucrose density-gradient ultracentrifugation (Leshchyns'ka and Sytnyk, 2013). We chose P0 because the axons are undergoing intense growth at this stage (Lewis *et al.*, 2013). We controlled our enrichment protocol by analyzing the cis-Golgi matrix protein (GM130) and the growth cone JNK-interacting protein 1 (JIP1) (Figure 3A). As expected (Dajas-Bailador et al., 2008), GM130 was mostly in the non-growth cone fraction, while JIP1 was enriched in the growth cone fraction.

This analysis yielded 2,873 different proteins identified with at least two peptides (Table S1). We compared this list of proteins with a reference growth cone proteome (Igarashi, 2014) and found that 97% of the major growth cone markers were present in our growth cone proteome from $Hdh^{Q7/Q7}$ and $Hdh^{Q7/Q111}$ mice (Table S2), but none differed in abundance between the two genotypes. Among the 2,873 proteins, 20 were less abundant and 8 more abundant in $Hdh^{Q7/Q111}$ growth cone preparations (Figure 3B, Table S1). These proteins belonged to six main functional categories (Table S3). The two major classes were DNA- and RNA-binding proteins, among which chromatin modifiers and transcription factors were the most abundant class that was downregulated in HD. Several other studies have highlighted the presence of transcription factors in the axon growth cone (Ji and Jaffrey, 2014; Suzuki et al., 2020), though a relationship

between transcription and axonal growth has yet to be established. We found several microtubule-, lipid- and ubiquitin-binding proteins and proteins involved in transport, e.g., KINECTIN1 (KTN1). Several cell adhesion proteins such as FAT atypical cadherin 4 (FAT4) were also differentially regulated in HD. We validated candidate proteins in each of these categories by immunoblotting growth cone-enriched fractions from P0 cortices of $Hdh^{Q7/Q7}$ and $Hdh^{Q7/Q111}$ mice (Figure 3C). We focused on the downregulated hits, because MS analysis detected only a small number of peptides for the upregulated ones (Table S1, column E). We then focused on proteins for which antibodies were available. We confirmed the downregulation of the transcription activator SMARCA4 and the structural maintenance of chromosomes flexible hinge domain-containing protein 1 (SMCHD1) but could not confirm KTN1 down-regulation in the HD growth cone (Figure 3C). Immunocytochemistry confirmed the strong down-regulation of FAT4 in the HD growth cone (Figure 3D).

Among these candidates, we were particularly interested in the microtubule-binding nuclear/mitotic apparatus protein, NUMA1 (Figure 3B) because it promised insight into the bundling defect that we observed in the HD growth cone: the C-terminal domain of NUMA1 has a stretch of 100 amino acids that directly binds and bundles microtubules (Haren and Merdes, 2002). NUMA1 protein levels were also 3.6-fold lower in HD mice than in controls; this result seems highly reliable since the protein was identified and quantified with 18 different peptides (Table S1). While NUMA1 has been shown to bundle microtubules during cell division (Forth et al., 2014; Gallini et al., 2016; Merdes et al., 1996), we postulated that it might be important for bundling during axonal growth. We verified NUMA1 expression by immunoblotting (Figure 3C) and found that NuMA1 protein levels were downregulated in the HD growth cone fraction, in agreement with our MS-based quantitative characterization.

miR-124 and protein degradation pathways lead to NUMA1 downregulation in HD

NUMA1 downregulation in P0 HD cortical growth cone fractions was proportional to its decrease in non-growth cone fractions that include cell bodies, axons and dendrites (Figure 4A). NUMA1 protein was also markedly decreased in both the nuclear and the cytosolic extracts of HD brains compared to control (Figure S2A). We then stained cortical neurons at DIV4 for the presence of NUMA1: NUMA1 staining was visible in the cell body, along neurites, and in the growth cone in controls (Figure 4B). NUMA1 levels were overall lower in all cellular

compartments of $Hdh^{Q7/Q111}$ than in $Hdh^{Q7/Q7}$ neurons (Figures 4A and 4B). These data suggest that the lower level of NUMA1 in the HD growth cone reflects a genuine decrease in abundance rather than a defect in the distribution of the protein.

To determine whether NUMA1 mRNA levels were deregulated in HD at the transcriptional or post-transcriptional level (Figure 4C), we performed reverse transcription quantitative PCR (rt-qPCR). NUMA1 mRNA levels were similar in P0 control and HD cortices, indicating that NUMA1 downregulation in HD occurs mostly at the post-transcriptional level. We decided to look for microRNAs (miRNAs), which have been closely linked to the post-translational regulation of almost all fundamental biological pathways, including axonal growth during cortical development (Wilson and Caceres, 2020). We performed an in silico analysis of mouse NUMA1 3'UTR using the biotool TargetScan and found 10 miRNA with putative binding sites in the 3'UTR of NUMA1. Among them, only miR-124 was significantly upregulated in HD compared to control cortices (Figure 4D). To see whether NUMA1 is a target of miR-124, we electroporated primary cultures of $Hdh^{Q7/Q111}$ neurons with antagomiR-124 (Figure 4E). Inhibiting miR-124 markedly increased NUMA1 in HD cells.

We also investigated the two main mechanisms of protein degradation, autophagy and the ubiquitin-proteasome system (UPS) (Figures S2B and S2C). We treated HD cortical neurons with bafilomycin or MG132 (lysosome and proteasome inhibitors, respectively). As expected, bafilomycin increased the levels of the autophagy adaptor protein p62, and treatment with MG132 increased ubiquitination overall. Both treatments augmented NUMA1 protein levels in HD compared to the non-treated conditions. There are probably several mechanisms at work to regulate NUMA1 protein levels in HD, with miR-124 acting upstream to suppress NUMA1 even before lysosomal or proteasomal degradation.

NUMA1 localizes to microtubules in the growth cones of cortical neurons

Because NUMA1 has never been reported to play a role in axonal development, we first investigated this possibility in control conditions. We immunoblotted extracts from primary cultures of cortical neurons at different DIV corresponding to different stages of maturation (Lewis *et al.*, 2013). NUMA1 expression remained constant during the first week of maturation (dendrite and axonal outgrowth) and decreased after DIV6, when neurons start to establish interneuronal connections (Figure 5A). This expression pattern was consistent with previous

studies (Ferhat et al., 1998; Torii et al., 2020) and suggests that NUMA1 plays a role in neuronal maturation.

We also stained cortical neurons in culture for the presence of NUMA1. In DIV3 neurons, NUMA1 was found in the cell body, along neurites and in the growth cone (Figure 5B, upper panels). We looked specifically at NUMA1 localization in axonal growth cones by immunostaining for the presence of TAU and F-ACTIN, which label axons and the growth cone periphery, respectively (Figure 5B, lower panels). NUMA1 staining was strong in the axonal shaft and in the growth cone but did not show obvious colocalization with F-ACTIN. We then analyzed NUMA1 distribution in regards to the microtubule cytoskeleton (Figure 5C). NUMA1 was particularly enriched in the main microtubule bundle. It also decorated the exploratory microtubules in the peripheral domain that contact the growth cone cortex. To confirm the association between NUMA1 and microtubules, we used a detergent extraction assay on cortical neurons to wash out proteins that are not associated with the cytoskeleton (Figure 5D). As expected, detergent treatment eliminated cytosolic GFP, whereas the endogenous NUMA1 signal remained in the growth cone where it strongly localized with the major microtubule bundle in the central domain. Confirming these observations, NUMA1 was enriched with polymerized microtubules in a microtubule co-sedimentation assay from protein extract of P0 cortical tissue (Figure S3).

Downregulation of NUMA1 recapitulates the HD defect in axonal outgrowth

We next investigated NUMA1's contribution to axonal outgrowth of callosal fibers in the P4 brain. Because NUMA1 is important for mitosis, cell polarization and migration (di Pietro et al., 2016; Jin et al., 2017; Torii *et al.*, 2020), anything that interfered with these functions would likely affect post-natal axonal growth. We therefore used in utero electroporation to decrease NUMA1 in postmitotic cells once they exit the cell cycle or once their migration is completed (Figure 6A). We first decreased NUMA1 in newborn neurons by electroporating lox-GFPshNUMA1 or lox-GFP only in E15.5 embryos with a plasmid expressing CRE under the control regulatory sequence of the NeuroD promoter (ND:CRE) (Figures 6A and B). In this way, NeuroD is expressed in newborn neurons but not in cycling progenitors or Tbr2-positive intermediate progenitors. Second, to target cells that have ended their migration, we electroporated E15.5 embryos with lox-GFPshNUMA1 or lox-GFP with a tamoxifen-dependent

ERT2-CRE construct so that CRE expression can be induced in P0 pups by tamoxifen injection (Figures 6A and 6C). Both conditions (NUMA1 decreased from embryonic or postnatal stages only) recapitulated the HD phenotype to the same extent, with callosal projections crossing the midline but being shorter than controls (Figures 6B and 6C). Thus, NUMA1 depletion during the postnatal period, independent of neuronal migration, is sufficient to affect axonal outgrowth of callosal fibers in vivo.

To decipher the mechanisms involved in NUMA1-induced deregulation of axonal outgrowth, we cultured E16.5 wild-type cortical neurons that were previously electroporated with mVenus at E15.5 (Figure S4A). Since NUMA1 contributes to axonal polarization (Torii *et al.*, 2020), we decreased the expression of NUMA1 by infecting cells with lentivirus expressing shRNA against the NUMA1 mRNA at late DIV1, when the cells are polarized and the axon specified in our primary cortical cultures. Immunoblotting revealed that NUMA1 was efficiently downregulated at DIV4 (Figure S4B). As in vivo, NUMA1-depleted callosal neurons in vitro had shorter axons (Figure S4C) and larger growth cones (Figure 6D) than control neurons. The main microtubule bundle in the central domain of the growth cone was markedly disorganized, and the exploratory microtubules in the peripheral domain grew longer (Figure 6E). Loss of NUMA1 thus recapitulates HD-induced defects in axonal growth and microtubule organization in the growth cone.

Expression of NUMA1 restores microtubule bundling and rescues HD-shortened axons

To determine whether HD-induced defects in axonal development are caused by the downregulation of NUMA1, we prepared primary cultures of cortical neurons from E16.5 $Hdh^{Q7/Q7}$ and $Hdh^{Q7/Q111}$ brains electroporated at E15.5 with a plasmid encoding cytosolic NUMA1 (i.e., NUMA1 without its nuclear localization signal) tagged with GFP (GFP-NUMA1) (Figure 7A). We next assessed whether NUMA1 promotes axonal growth in HD through its ability to bind and organize the microtubule arrays. For that purpose, we expressed a plasmid encoding a version of the NUMA1 protein in which the microtubule-binding domain was deleted (GFP-NUMA1-ΔMBD) (Figure 7A) (Gallini *et al.*, 2016).

As expected, using a detergent extraction assay as before (Figure 5D), GFP-NUMA1 remained associated with the microtubule cytoskeleton while GFP-NUMA1-ΔMBD did not (Figure 7B). We used the status of the central microtubule bundle in growing axons as a read-out

of the HD phenotype, since the integrity of this structure is required for proper axonal growth. HD neurons again showed defective bundling of the central microtubule domain (Figure 7C), but GFP-NUMA1 expression was sufficient to rescue microtubule bundling and restore axonal growth (Figure 7D). In contrast, GFP-NUMA1-ΔMBD exacerbated the axonal defect (Figure 7D). Thus, the microtubule-binding domain of NUMA1 is required to regulate axonal growth.

Antagomir-124 expression and epothilone B treatment restore axonal growth in HD mice

Finally, to see if we could prevent the HD-induced defects in vivo, we restored NUMA1 protein levels by electroporating GFP-NUMA1 in E15.5 $Hdh^{Q7/Q111}$ embryos and measuring the axons at P0 (Figure 8A). (NUMA1's size, 250kDa, prevented us from expressing it by postnatal viral injections.) Callosal fibers in HD neurons expressing GFP-NUMA1 grew as long as those in controls.

We also restored NUMA1 expression postnatally by using antagomiR-124 (Figure 8B). We injected antagomiR-124 in the facial vein of P0 $Hdh^{Q7/Q111}$ animals and analyzed the axonal growth of callosal fibers at P4. HD callosal fibers treated with antagomiR-124 grew as long as the controls (Figure 8A). Electroporating antagomiR-124 in E15.5 HD embryos produced a similar rescue (Figure S5A). Together with our results on NUMA1 downregulation in E15.5 $Hdh^{Q7/Q7}$ and NUMA1 expression in E15.5 $Hdh^{Q7/Q111}$ (Figures 6A-6C and 8A), this strongly supports the idea that the mechanisms by which antagomir-124, NUMA1 and mutant HTT regulate axonal growth are independent of neuronal migration.

Finally, we targeted the microtubule defect in HD using epothilone B, a microtubule-stabilizing drug. Epothilone B crosses the blood-brain barrier and has been used to promote axonal regeneration in mouse (Kugler et al., 2020; Ruschel et al., 2015). In HD cortical neurons in culture, epothilone B treatment restored the organization of the main microtubule bundle in the central domain of the growth cone (Figure S5B). We also injected epothilone B subcutaneously in P0 $Hdh^{Q7/Q111}$ animals and analyzed callosal fibers at P4 (Figure 8B). Epothilone B-treated HD animals grew callosal fibers as long as controls.

Therefore, the limited axonal growth in early HD can be rescued by NUMA1 expression, which restores the organization of the microtubule array in the growth cone.

DISCUSSION

A thin callosum and attenuated connectivity between the two cortical hemispheres can be observed decades before the first clinical symptoms of HD in mutation carriers (reviewed in (Estevez-Fraga *et al.*, 2020)). We show that these early defects arise from impaired axonal growth during development, rather than through a degenerative process. The growth of callosal axons is compromised in HD mice from P0; at P4, callosal fibers are able to cross the corpus callosum but still show delayed outgrowth compared to the control condition. This axonal growth deficiency has two major consequences for the maturation of cortical connections. First, a proportion of HD axons fails to reach the contralateral side to establish connections at all. Second, the fibers that reach their final destination augment their branching within layers II/III and V, but this is insufficient to compensate for the diminished cortical ramifications. The branching defect in HD could also result from the fibers arriving on the contralateral side too late to receive the proper signals.

Deepening our understanding of trafficking defects in HD

HD is rightfully considered a disease of impaired trafficking, but the present study shows that HD affects the cytoskeletal infrastructure itself. HTT has been known for some time to rely on microtubules for not just axonal transport of vesicles, but also other functions in ciliogenesis and mitotic spindle orientation, all of which are altered in HD (Saudou and Humbert, 2016). Whether HD interferes with microtubule organization and dynamics has been largely unknown. We previously showed that the dynamic instability of microtubules was diminished in HD mouse embryonic fibroblasts, and that they persisted abnormally after membrane contact (Molina-Calavita *et al.*, 2014). It is now clear that in HD the microtubule array in the growth cone is itself disorganized, with impaired microtubule bundling in the central domain and longer exploratory microtubules in the peripheral domain, resulting in an overall increased growth cone area. As the growth cone advances, the peripheral domain becomes the new central domain while the previous central domain, in turn, gives rise to the axonal shaft by constricting the growth cone and bundling microtubules, resulting in a net elongation of the axon (Pinto-Costa and Sousa, 2021). Thus, the disorganization of microtubules observed in the growth cone of HD callosal neurons contributes to their poor elongation, which can be rescued in vivo by the microtubule

stabilizing agent epothilone B. Determining whether microtubule disorganization also contributes to the impairment of microtubule-based functions of HTT will require further study.

Unexpected functions for NUMA1 in microtubule organization and axonal growth

Most studies on NUMA1 have focused on its role in spindle formation and orientation (di Pietro *et al.*, 2016). During spindle assembly, the interaction of NUMA1 with dynein/dynactin promotes microtubule tethering to the poles; in metaphase, NUMA1 binds to dynein/dynactin and to the leucine-glycine-asparagine LGN protein to recruit dynein to the cortex, where it exerts attractive forces on astral microtubules for cell division. NUMA1 also binds directly to microtubules and leads to the formation of stable bundles during division (Forth *et al.*, 2014; Gallini *et al.*, 2016; Haren and Merdes, 2002; Merdes *et al.*, 1996). Here, we show that NUMA1, by directly binding to microtubules, also organizes the central microtubule bundles in the growth cone.

Only a few studies have investigated the role of NUMA1 in differentiating and mature neurons. Ferhat and colleagues observed NUMA1 in the cell body of developing sympathetic and hippocampal neurons (Ferhat *et al.*, 1998). They found that NUMA1 protein levels increased during the first days in vitro before decreasing at later stages (as we also found) and suggest that NUMA1 could be a component of the somatodendritic microtubule arrays of the neurons (Ferhat *et al.*, 1998). More recent studies highlight the role of NUMA1 in the development of cortical neurons. NUMA1 cooperates with the non-catalytic regulatory p80 subunit of katanin, whose mutation causes microlissencephaly (Jin *et al.*, 2017), to regulate not only cortical neurogenesis but also the radial migration of newly generated neurons. NUMA1 is also required at a later stage of neuronal development during the assembly of the axonal initial segment (Torii *et al.*, 2020). NUMA1 inhibits Neurofascin endocytosis, leading to its accumulation on the plasma membrane and promoting the enrichment of other proteins of the axonal initial segment and its stabilization (Torii *et al.*, 2020). Once the axon initial segment is stabilized, NUMA1 is no longer required for its maintenance. We now show that NUMA1 is essential for growth cone integrity and axonal growth independent of its role in neurogenesis, migration and polarization.

During neuronal maturation in HD, NUMA1 protein levels are severely downregulated by miR124; the remaining levels of NUMA1 in HD can be increased by treatment with ubiquitin and autophagy inhibitors. Interestingly, Eshraghi et al. recently reported that mutant HTT stalls

ribosomes, globally repressing protein synthesis—including that of NUMA1 (Eshraghi et al., 2021). Along similar lines, or at least to similar effect, the cellular stress that occurs in HD also downregulates NUMA (Jayaraman et al., 2017). In these studies, the authors propose that the mechanisms involve the interaction of mutant HTT and NUMA1 with ribosomal proteins. Whether such mechanisms could also contribute to the downregulation of NUMA1 in HD neuronal maturation remains to be tested.

An integrated model of early development in HD

Because the striatum is the first region to show neuronal loss in HD (Rub et al., 2016), the contribution of the cerebral cortex to HD has been relatively neglected. Accumulating evidence supports the notion that the striatal degeneration is, in fact, caused by defective cortical signaling to the striatum (Tereshchenko *et al.*, 2020; Virlogeux et al., 2018; Wang et al., 2014; Zhao et al., 2016). Neurons projecting to the striatum (layer V neurons) are particularly susceptible in HD patients (Hedreen et al., 1991), and cortical layer II/III neurons that project through the corpus callosum to the contro-lateral hemisphere also degenerate in HD patients (Hedreen *et al.*, 1991). Thus, similar to what has been proposed for the cortico-striatal connection, the reduced cortico-cortical connectivity shown here could explain the thin corpus callosum observed in presymptomatic gene carriers.

We show that the growth of callosal axons is compromised in HD mice. Whether the number of upper layer neurons and their migration is also affected in HD is not clear (Barnat *et al.*, 2017; Molina-Calavita *et al.*, 2014). It could well be the case, given that wild-type HTT regulates the maintenance of their pool and their migration (Barnat *et al.*, 2017; Tong et al., 2011); this would precede the axonal growth defect and could influence it, although part of the impairment in axonal growth involves a cell-autonomous mechanism, as indicated by axonal growth defects of HD callosal neurons in cell cultures. It is worth noting that HD callosal neurons showed branching defects in vivo but not when they were isolated in cell cultures. This suggests that the defective branching on the contralateral side is not due to an autonomous mechanism but rather that these HD axons are not exposed to the proper extracellular signaling. As noted above, this may be a matter of timing. It is also possible, however, that there are abnormalities in extracellular signaling in HD that also contribute to the impaired branching.

It is now clear that HD interferes with the fundamental processes of cortical development:

neurogenesis (Barnat *et al.*, 2020), neuronal migration (Barnat *et al.*, 2017), and (from the current study) axonal growth and maturation into the proper circuit. A young mature HD brain has fewer neurons than a control one; not all neurons will reach their final destination, and for those that do, their connectivity is altered. These subtle deficits form the substrate for subsequent compensatory events, prodromal clinical signs and degeneration.

Precisely how each defective stage interferes with the subsequent one, with additive or compensatory effects, remains to be established. It is of the utmost importance to consider HD longitudinally and to differentiate between pathogenic and compensatory changes so that therapies can be directed against the former while promoting, or at least not undermining, the latter (Al-Ramahi et al., 2018). The exact contribution of abnormal development to adult pathology also needs to be well-mapped, so that we can integrate neurodevelopment in our therapeutic strategies. Our data here create at least a theoretical possibility that therapies delivered very early in life could delay the onset of classic HD symptoms.

ACKNOWLEDGMENTS

We kindly thank Béatrice Blot and staff of animal facilities (GIN) for technical support; Monia Barnat for discussions; Julien Le Friec for sharing samples; Sophie Lenoir for help with animal experimentation; the GIN imaging facility platform (PIC-GIN) for help with image acquisitions; Vicky Brandt and Frédéric Saudou for helpful comments on the manuscript. This work was supported by grants from Agence Nationale pour la Recherche (ANR-15-IDEX-02 NeuroCoG in the framework of the “Investissements d’avenir” program, S.H.; AXYON: ANR-18-CE16-0009-01, S.H.), Fondation pour la Recherche Médicale (FRM, équipe labellisée DEQ20170336752, S.H.; PhD fellowship, FDT202001010865, R.C.), AGEMED program from INSERM (S.H.). Proteomic experiments were partly supported by ANR under projects ProFI (Proteomics French Infrastructure, ANR-10-INBS-08) and GRAL, a program from the Chemistry Biology Health (CBH) Graduate School of University Grenoble Alpes (ANR-17-EURE-0003).

AUTHOR CONTRIBUTIONS

M.C. and S.H. designed the study and wrote the manuscript, which was commented on by all authors. M.C. performed most of the experiments and data analyses. R. C. performed co-sedimentation assay, permeabilization assay and participated to mass spectrometry sample

preparation. R.K. performed rt-qPCR experiments and analyses; E. D. generated tools for image analyses and performed analyses. A. A. and Y. C. performed quantitative proteomic analyses. M.M. provided expertise and reagents.

DECLARATION OF INTERESTS

The authors declare no conflict of interest.

FIGURE LEGENDS

Figure 1. Axonal Growth and Branching are Impaired in HD Mice.

(A) Selective labeling of layer II/III neurons with membrane-RFP (Mem-RFP) by electroporation at E15.5 and post-natal axonal length measurement. The arrow indicates the end of the axon tract.

(B) Representative coronal sections of P0 and P4 $Hdh^{Q7/Q7}$ and $Hdh^{Q7/Q111}$ cortices with magnification of the corpus callosum for P0. Histograms compare axonal length. P0 unpaired t-test, **p=0.0076 ($Hdh^{Q7/Q7}$: 1625 ± 70.7; $Hdh^{Q7/Q111}$: 1353 ± 64.22; n=17 brains for each condition). P4, unpaired t-test, ***p=0.0004 ($Hdh^{Q7/Q7}$: 4423 ± 202.2; $Hdh^{Q7/Q111}$: 3384 ± 170.8; n=18 brains for each condition). Error bars, SEM.

(C) Using the same electroporation scheme, we analyzed four regions of interest (numbered 1 to 4) at P21 in (D) and (E) and in Fig. S1 (B) and (C).

(D) Representative images of coronal sections of P21 $Hdh^{Q7/Q7}$ and $Hdh^{Q7/Q111}$cortices showing the corpus callosum. Line-scan analysis shows signal intensity (in arbitrary units, a.u.) along the corpus callosum (region 3). The shaded region represents SEM.

(E) Representative images of coronal sections of the contralateral side in P21 $Hdh^{Q7/Q7}$ and $Hdh^{Q7/Q111}$ cortices. The line-scan analysis shows signal intensity along layer II/III from the parietal to the auditory cortex (region 4). The shaded region represents SEM.

Figure 2. Growth Cone Morphology and Microtubule Organization are Modified in HD.

(A) Schematic of E16.5 primary cell culture of layer II/III neurons that are labeled with mVenus (green) by in utero electroporation at E15.5; at DIV4, mVenus-positive neurons are immunostained for SATB2 and CTIP2. The graph quantifies double-positive mVenus-SATB2 and mVenus-CTIP2 cells. Paired t-test, *p=0.035 (SATB2: 79.03 % ± 7.08; CTIP2: 12.41% ±

6.90; n=3 independent experiments for each condition).
(B) Representative $Hdh^{Q7/Q7}$ and $Hdh^{Q7/Q111}$ neurons. Axon lengths compared at right by Mann Whitney-test, ****p<0.0001 ($Hdh^{Q7/Q7}$: median 273.5; $Hdh^{Q7/Q111}$: median 244.9; n= at least 425 axons from 5 independent experiments for each condition). Primary branches for 100 µm of axon in each genotype were compared by unpaired t-test, p=0.798 ($Hdh^{Q7/Q7}$: median 0.4132; $Hdh^{Q7/Q111}$: 0.3905; n= at least 45 axons from 4 independent experiments for each condition).
(C) Representative confocal Airyscan images of growth cones immunolabeled with phalloidin (ACTIN, green) and anti-tyrosinated TUBULIN antibody (tyr-TUB, grey). Growth cone areas by genotype compared by Mann Whitney-test, **p=0.002 ($Hdh^{Q7/Q7}$: median 59.17; $Hdh^{Q7/Q111}$: median 79.43; n= at least 91 growth cones from 4 independent experiments for each condition).
(D) Representative confocal Airyscan images of growth cones immunolabeled with anti-tyr-TUB antibody. Representative line-scan analysis (relative fluorescence intensity) and quantification of tyr-TUB maximum fluorescence intensity in the two genotypes by Mann Whitney-test, **p=0.002 ($Hdh^{Q7/Q7}$: median 92.03; $Hdh^{Q7/Q111}$: median 51.058; n= at least 30 growth cones from 3 independent experiments for each condition). Lengths of exploratory microtubules in the two genotypes compared by Mann Whitney-test, ****p<0.0001 ($Hdh^{Q7/Q7}$: median 3.34; $Hdh^{Q7/Q111}$: median 4.59; n= at least 98 exploratory microtubules from 4 independent experiments for each condition). Error bars, SEM.

Figure 3. Proteomic Analysis Highlights Alterations in Growth Cone Proteins in HD.
(A) HTT, GM130 and JIP1 immunoblotting analyses of non-growth cone (NGC) and growth cone (GC) fractions of $Hdh^{Q7/Q7}$ and $Hdh^{Q7/Q111}$ cortices.
(B) Volcano plot displaying the differential abundance of proteins in $Hdh^{Q7/Q7}$ and $Hdh^{Q7/Q111}$ growth cone preparations analyzed by MS-based quantitative proteomics. The volcano plot represents the $-\log_{10}$ (*limma* p-value) on the y-axis plotted against the $\log_2$ (Fold Change $Hdh^{Q7/Q7}$/$Hdh^{Q7/Q111}$ growth cones) on the x-axis. Green and purple dots represent proteins more abundant in $Hdh^{Q7/Q7}$ or $Hdh^{Q7/Q111}$ mice, respectively (five biological replicates, $\log_2$ Fold Change ≥ 0.67 or ≤ -0.67, p-value ≤ 0.01; Benjamini-Hochberg FDR < 5%).
(C) Immunoblotting analyses of growth cone (GC) fractions for NUMA1, SMARCA4, SMCHD1, KINECTIN1, and VINCULIN, quantified on the right as amount in $Hdh^{Q7/Q111}$ cortices expressed as percent of $Hdh^{Q7/Q7}$ in n=5 paired experiments. Paired t-test, ***p=0.0003

(NUMA1, mean of difference: -60 ± 5.021); *p=0.021 (SMARCA4, mean of difference: 41.39 ± 11.27); **p=0.0015 (SMCHD1, mean of difference: 54.41 ± 7.08); p=0.71 (KINECTIN1, mean of difference: 6.65 ± 16.51).

(D) Representative confocal images of growth cones immunostained for FAT4 (red). Histogram to the right shows FAT4 fluorescence intensity. Unpaired t-test, *p=0.01 ($Hdh^{Q7/Q7}$: 639.2 ± 63.98; $Hdh^{Q7/Q111}$: 388.7 ± 70.32; n= at least 5 growth cones from 3 independent experiments for each condition). Error bars, SEM.

Figure 4. NUMA1 Expression is Decreased in HD by miR-124.

(A) Immunoblotting for NUMA1, VINCULIN, GM130 and JIP1 in non-growth cone (NGC) and growth cone (GC) fractions. Histogram to the right quantifies NUMA1 in the GC fraction and, at the far right, in the GC fraction relative to the NGC fraction of both genotypes, in at least 5 independent experiments for each condition. Unpaired t-test, *p=0.017 ($Hdh^{Q7/Q7}$: 1.35 ± 0.12; $Hdh^{Q7/Q111}$: 0.912 ± 0.122); ns (p=0.43, $Hdh^{Q7/Q7}$: 0.91 ± 0.07; $Hdh^{Q7/Q111}$: 0.817 ± 0.096).

(B) Representative confocal images of cortical neurons at DIV4 and magnification of $Hdh^{Q7/Q7}$ and $Hdh^{Q7/Q111}$ growth cones immunolabeled with anti-NUMA1 antibody (grey) and phalloidin (green, to show ACTIN). The graph shows NUMA1 fluorescence intensity in both genotypes across 3 paired experiments. Paired t-test, *p=0.04 (mean of difference between $Hdh^{Q7/Q7}$ and $Hdh^{Q7/Q111}$: 41.7 ± 3.335).

(C) The graph shows NUMA1 mRNA expression analyzed by quantitative RT-qPCR in P0 cortices. Relative quantification was measured by means of the comparative cycle threshold (ΔΔCt) method. Paired t-test, p=0.37 ($Hdh^{Q7/Q111}$, mean of difference: 0.14 ± 0.14; n=6 independent experiments).

(D) The graph shows miRNA expression analyzed by quantitative RT-qPCR in P0 cortices, using the comparative cycle threshold (ΔΔCt) method. Paired t-test, p=0.1 (miR-7, mean of difference: 0.68 ± 0.36); *p=0.037 (miR-124, mean of difference: 0.48 ± 0.18); p=0.1 (miR-22, mean of difference: 0.16 ± 0.09); p=0.1 (miR-125, mean of difference: 0.65 ± 0.37); p=0.1 (miR-130, mean of difference: 0.33 ± 0.17); p=0.2 (miR-31, mean of difference: 0.84 ± 0.56); p=0.3 (miR-301, mean of difference: 0.25 ± 0.21); p=0.3 (miR-351, mean of difference: 0.14 ± 0.13); p=0.3 (miR-152, mean of difference: 0.15 ± 0.13); p=0.1 (miR-148b, mean of difference: 0.55 ± 0.30).

(E) NUMA1 and VINCULIN immunoblotting in DIV4 $Hdh^{Q7/Q7}$ and $Hdh^{Q7/Q111}$ cortical neurons treated as indicated. NUMA1 was assessed 72h after transfection. Graph to the right shows NUMA1 protein levels in $Hdh^{Q7/Q111}$ neurons as percent of its level in control neurons. One-way ANOVA, Tukey's multiple comparisons test, **p=0.0077 (mean of difference between $Hdh^{Q7/Q7}$ and $Hdh^{Q7/Q111}$: 0.4); p=0.06 (mean of difference between $Hdh^{Q7/Q7}$ and $HdhQ^{7/Q111}$+AntagomiR-124: -0.18); *p=0.01 (mean of difference between $HdhQ^{7/Q111}$ and $HdhQ^{7/Q111}$+AntagomiR-124: -0.59; n=4 independent experiments for each condition).
Error bars, SEM.

Figure 5. NUMA1 is Enriched on Microtubules in Growth Cones.

(A) NUMA1 and VINCULIN immunoblotting analysis at indicated DIV. The graph corresponds to the quantitative evaluation of NUMA1 protein in $Hdh^{Q7/Q7}$ cortical neurons express in percent of DIV1. One-way ANOVA with multiple comparisons followed by Dunnett's post hoc test, **p=0.002 (DIV8: -72.85 ± 5.35).
(B) Representative neurons immunostained for F-ACTIN (green), TAU-1 (magenta) and NUMA1 (grey). All confocal images taken with Airyscan.
(C) Representative growth cones immunostained for NUMA1 (grey), tyr-TUB (magenta) and F-ACTIN (green).
(D) Representative growth cones immunostained for GFP (green), NUMA1 (grey) and tyr-TUB (magenta). Before immunostaining, neurons were treated (+TritonX100) or not with detergent to extract soluble proteins. Line-scan analyses show fluorescence intensities of NUMA1 and tyr-TUB staining; graphs represent at least 5 growth cones for 3 independent experiments for each condition. Unpaired t-test, **p=0.003 (GFP no treatment: 100 ± 14.77; +TritonX100: 17.18 ± 1.545), **p=0.002 (tyr-TUB no treatment: 100 ± 10.12; +TritonX100: 177 ± 20.83), p=0.136 (NUMA11 no treatment: 100 ± 8.00; +TritonX100: 124 ± 14.83).
Error bars, SEM.

Figure 6. NUMA1 Depletion Impairs Axonal Growth.

(A) Procedure to delete NUMA1 in layer II/III neurons from embryonic neuronal differentiation to P4 or from the end of neuronal migration (P0) to P4. The control was wild-type mice electroporated with ND-CRE +lox-GFP or CRE-ERT2 + lox-GFP.

(B) Representative coronal sections of P4 ND:CRE + lox-GFP and ND:CRE + lox-GFPshNUMA1 cortices. Histograms quantify axonal length. Unpaired t-test, **p=0.001 (ND:CRE + Lox-GFP: 4886 ± 163.7 n=14; ND:CRE + lox-GFPshNUMA1: 4060 ± 145.2; n=12 brains for each condition).

(C) Representative coronal sections of P4 CRE-ERT2 + lox-GFP and CRE-ERT2 + lox-GFPshNUMA1 cortices. Histograms quantify axonal length. Unpaired t-test, ***p=0.0008 (CRE-ERT2 + Lox-GFP: 4953 ± 110.6; CRE-ERT2 + lox-GFPshNUMA1: 4017 ± 214; n=12 brains for each condition).

(D) Representative confocal images of growth cones immunolabeled with phalloidin (ACTIN, green) and anti-tyrosinated TUBULIN antibody (tyr-TUB, grey). The graph compares growth cone areas in control (CT) and NUMA1-depleted (shNUMA1) conditions. Unpaired t-test, ***p=0.0001 (control: median 139.1; shNUMA1: median 228.3; n= at least 10 growth cones from 4 independent experiments for each condition).

(E) Representative confocal Airyscan images of growth cones immunolabeled with anti-tyr-TUB antibody show effects of NUMA1 suppression. Left histogram: Representative line-scan analysis (relative fluorescence intensity). Right histogram: lengths of exploratory microtubules. Mann Whitney-test, ****p<0.0001 (control: median 3.17; shNUMA1: median 4.58; n= at least 172 exploratory microtubules from 4 independent experiments for each condition).

Error bars, SEM.

Figure 7. NUMA1 Expression Rescues the Axonal Defect of HD Cortical Neurons in Culture.

(A) Schematic of NUMA1 constructs. NLS, nuclear localization signal; MBD, microtubule-binding domain.

(B) Representative confocal images of GFP-stained cortical neurons expressing the indicated constructs. Before immunostaining, neurons were treated (+TritonX100) or not to extract soluble proteins. In this panel, GFP-NUMA1ΔMBD is abbreviated as GFP-NUMA1Δ.

(C) Representative confocal Airyscan images of growth cones immunostained with anti-GFP (green) and anti-tyrosinated TUBULIN (tyr-TUB, grey) antibodies. Below: Representative line-scan analyses of relative fluorescence intensity.

(D) Representative $Hdh^{Q7/Q7}$ and $Hdh^{Q7/Q111}$ neurons expressing the indicated constructs. Histograms show axonal lengths. One-way ANOVA with multiple comparisons followed by Tukey's post hoc test, **p=0.0051 (mean of difference between $Hdh^{Q7/Q7}$ and $Hdh^{Q7/Q111}$ 39.57); p=0.999 (mean of difference between $Hdh^{Q7/Q7}$ and $Hdh^{Q7/Q111}$ + NUMA1: 1.46); ****p<0.0001 (mean of difference between $Hdh^{Q7/Q7}$ and $Hdh^{Q7/Q111}$ + NUMA1ΔMBD: 119); **p=0.0035 (mean of difference between $Hdh^{Q7/Q111}$ and $Hdh^{Q7/Q111}$ + NUMA1: -38.11); ****p<0.0001 (mean of difference between $Hdh^{Q7/Q111}$ and $Hdh^{Q7/Q111}$ + NUMA1ΔMBD: 76.46); ****p<0.0001 (mean of difference between $Hdh^{Q7/Q111}$ + NUMA1 and $Hdh^{Q7/Q111}$ + NUMA1ΔMBD: 117.6). n=at least 132 axons from 4 independent experiments for each condition.
Error bars, SEM.

Figure 8. NUMA1 Expression and Microtubule Stabilization Rescues Axonal Length of HD Cortical Neurons in Vivo

(A) Representative coronal sections of P0 $Hdh^{Q7/Q7}$ and $Hdh^{Q7/Q111}$ cortices expressing GFP or GFP-NUMA1. Histogram quantifies axon length in the three conditions. One-Way ANOVA with multiple comparisons followed by Tukey's post hoc test, *p=0.041 (mean of difference between $Hdh^{Q7/Q7}$ and $Hdh^{Q7/Q111}$: 493.9); **p=0.008 (mean of difference between $Hdh^{Q7/Q111}$ and $Hdh^{Q7/Q111}$ + NUMA1: 653.8); p=0.721 (mean of difference between control and $Hdh^{Q7/Q111}$ + NUMA1: 160). n=at least 132 axons from 4 independent experiments for each condition.
(B) Schematic of experimental procedure to recover $Hdh^{Q7/Q111}$ axonal growth of layer II/III neurons from P0 to P4. For each condition the embryos were electroporated with Mem-RFP at E15.5. The P0 Mem-RFP positive pups were injected with PBS for $Hdh^{Q7/Q7}$ and $Hdh^{Q7/Q111}$, with PBS + antagomiR-124 for $Hdh^{Q7/Q111}$ or PBS + epothilone B for $Hdh^{Q7/Q111}$. Representative coronal sections of P4 $Hdh^{Q7/Q7}$ and $Hdh^{Q7/Q111}$ cortices expressing Mem-RFP and treated with antagomiR-124 or epothilone B. Histograms below show axon lengths in each condition. One-way ANOVA, Tukey's multiple comparisons test, ****p<0.0001 (mean of difference between $Hdh^{Q7/Q7}$ and $Hdh^{Q7/Q111}$: 1192 µm); p>0.99 (mean of difference between $Hdh^{Q7/Q7}$ and $HdhQ^{7/Q111}$ + antagomiR-124: -28.83 µm); p=0.26 (mean of difference between $Hdh^{Q7/Q7}$ and $HdhQ^{7/Q111}$ + epothilone B: 434.4 µm); ****p<0.0001 (mean of difference between $HdhQ^{7/Q111}$ and $HdhQ^{7/Q111}$ + antagomiR-124: -1221 µm); **p=0.0057 (mean of difference between $HdhQ^{7/Q111}$ and $HdhQ^{7/Q111}$ + epothilone B: -757.5 µm); p=0.22 (mean of difference between

HdhQ$^{7/Q111}$+antagomiR-124 and HdhQ$^{7/Q111}$ + epothilone B: -463 µm) n=12 brains from 4 independent experiments for each condition.

Error bars, SEM.

STAR★METHODS

Detailed methods are provided in the online version of this paper and include the following:

- **KEY RESOURCES TABLE**
- **CONTACT FOR REAGENT AND RESOURCE SHARING**
- **EXPERIMENTAL MODEL AND SUBJECT DETAILS**
- **METHOD DETAILS**
  - In utero electroporation, brain fixation and cell culture
  - Neonatal mouse treatment
  - Cell treatment
  - Immunocytochemistry
  - Growth cone fractionation
  - Mass spectrometry-based proteomic analyses
  - Microtubule co-sedimentation assay
  - Nuclear and cytoplasmic proteins extraction
  - Quantitative real-time PCR (qPCR)
  - Plasmids
  - Image acquisition
- **QUANTIFICATION AND STATISTICAL ANALYSIS**

STAR ★METHODS

KEY RESOURCES TABLE

REAGENT or RESOURCE	SOURCE	IDENTIFIER
Antibodies		
anti-Tyrosinated TUBULIN (YL1/2, Tyr-TUB)	Provided by M.-J. Moutin, Grenoble Institute Neuroscience	N/A
anti-NUMA1	Abcam	Cat#ab109262
anti-atto-488-phalloidin	Sigma-Aldrich	Cat#49409
anti-SATB2	Abcam	Cat#ab51502
anti-CTIP2	Abcam	Cat#ab18465
anti-VINCULIN	Sigma	Cat#V9131
anti-JIP1(B-7)	Santa Cruz Biotechnology	Cat#sc-25267
anti-GM130	BD Transduction Laboratories	Cat#610822
anti-KINECTIN1	Genetex	Cat#GTX66105
anti-FAT4	Thermo Fisher	Cat#PAS-72970
anti-SMCHD1	Novus Biologicals	Cat#NBP1-82978
anti-SMARCA4	Abcam	Cat#ab110641
anti-LAMINB1	Abcam	Cat#ab133741
anti-poly Ubiquitin		Cat#
anti-p62	Sigma	Cat#P0067
anti-TAU	Abcam	Cat#ab75714
anti-α-TUBULIN	Sigma	Cat#T9026
anti-GFP	Abcam	Cat#ab13970
donkey anti-mouse IgG (H+L) - Cy™2 conjugate	Jackson ImmunoResearch	Cat#715-225-151
donkey anti-mouse IgG (H+L) - Cy™3 conjugate	Jackson ImmunoResearch	Cat#715-225-150
donkey anti-rat IgG (H+L) - Cy™5 conjugate	Jackson ImmunoResearch	Cat#715-175-151
goat anti-rabbit IgY (H+L) - Alexa Fluor® 555 conjugate	Thermofisher scientific	Cat#A21428
goat anti-mouse IgG1 - HRP conjugate	SouthernBiotech	Cat#1070-05
donkey anti-mouse IgG H&L (HRP)	Abcam	Cat#ab6820
Bacterial and Virus strains		

LV.pLKO1-shNUMA1mm-GFP	(Gallini *et al.*, 2016)	N/A
LV.pLKO1-gfp	(Gallini *et al.*, 2016)	N/A
Chemicals, Peptides, and Recombinant Proteins		
Hoechst 33342	ThermoFisher	Cat#H3570
Dako Fluorescent mounting medium	Agilent	Cat#S302380-2
Proteases Inhibitor	Sigma-Aldrich	Cat#P8340
Phosphatases Inhibitor	Sigma-Aldrich	Cat#P5726
Triton X-100	Sigma-Aldrich	Cat#X100-500ML
pCALNL-GFP-U6-shNUMA1	This paper	N/A
pCALNL-GFP	Addgene	Cat#13770
pCAG-ERT2creERT2	Addgene	Cat#13777
pNeuroD-IRES-CRE-GFP (ND: CRE)	Provided by L. Nguyen, University of Liège, Belgium.	N/A
pCAGGS-NLS-GFP	Provided by L. Nguyen, University of Liège, Belgium.	N/A
AntagomiR-124	Qiagen	Cat#339132
EpothiloneB	Div Bio Science	Cat#S1364
Bafilomycin	Sigma	Cat#B1793
MG132	Sigma	Cat#474790
Tamoxifen	Sigma	Cat# T5648
PFA formaldehyde 32%	Euromedex	Cat#15714-S
Taxol/Paclitaxel	Sigma-Aldrich	Cat#T7191
glutaraldehyde solution 25%	Sigma-Aldrich	Cat#G5882-50ML
Sodium borohydride	Sigma-Aldrich	Cat#452874
Porcine tubulin	TEBU BIO	Cat#T240-A
Recombinant DNA		
pCAG_GFP	(Barnat *et al.*, 2017)	N/A
pCAG_GFP-NUMA1ΔNLS	This paper	N/A
pCAG_GFP-NUMA1ΔNLSΔMBD	This paper	N/A

pCAG-mVENUS (pSCV2)	Provided by J. Courchet, Neuromyogene, Lyon, France	N/A
pCAG-TdTomato-1C-HS1BGFP-SV40pA	Addgene	Cat#26771
Experimental Models: Organisms/Strains		
SWISS-CD1	Janvier Lab	
Hdh$^{Q7/Q111}$	Provided by M.-F. Chesselet, UCLA, US.	
Hdh$^{Q7/Q175}$	The Jackson Lab	B6J.129S1-Htttm1Mfc/190ChdiJ
Software and Algorithms		
Image J/Fiji	NIH	https://imagej.nih.gov/ij/download.html
Adobe Illustrator		
Graph pad Prism 7.0		
Deposited Data		
Mass spectrometry data	ProteomeXchange repository	http://www.proteomexchange.org/, dataset identifier PXD023885

RESOURCE AVAILABILITY

Lead contact

Further information and requests for resources and reagents should be directed to and will be fulfilled by the Lead Contact, Sandrine Humbert (sandrine.humbert@univ-grenoble-alpes.fr).

Materials availability

All unique/stable reagents generated in this study are available from the Lead Contact without restriction.

EXPERIMENTAL MODEL AND SUBJECT DETAILS

Hdh$^{Q111/Q111}$ mice are in a CD1 background and Hdh$^{Q7/Q175}$ in a C57BL/6J background. All mice are derived from heterozygous crosses. All experimental procedures were performed in authorized establishments (Grenoble Institute of Neurosciences, INSERM U1216, license #B3851610008) in strict accordance with the local animal welfare committee (Comité Local

Grenoble Institute Neurosciences, C1EA-04), EU guidelines (directive 2010/63/EU) and the French National Committee (2010/63) for care and use of laboratory animals.

METHOD DETAILS

In utero electroporation, brain fixation and cell culture

E15.5 embryos were electroporated in utero with 2 µg/µl of the plasmids of interest as previously described (Barnat *et al.*, 2017). mem-RFP or Venus-positive cortices were either fixed or dissociated for cell culture, respectively. For cell culture, Venus-positive cortices were harvested at E16.5, dissected, and digested in Papain enzyme solution. Papain was inactivated using FBS (10%) and cells were washed with opti-MEM-glucose. Cells were cultured on poly-L-lysine matrices in Neurobasal supplemented with B27 (2%), glutamax (1%), and Penicillin/Streptomycin (1%). The cells were plated at a density of 800,000 cells/well in 6-well plates and fixed at DIV4.

Mem-RFP positive animals were intracardiacally perfused with PBS followed by cold paraformaldehyde (PFA) 4%. Brains were harvested, post-fixed overnight in PFA 4% and sectioned (300 µm) through the entire somatosensory cortex. After 3 rinses in PBS, slices were mounted in Dako mounting medium.

Neonatal mouse treatment

All the treatments were performed in P0 mice. Tamoxifen (Sigma, 100 mg/kg) and epothilone B (Div Bio Science, 0.75 mg/kg) were injected subcutaneously. The antagomiR-124 (Qiagen, 300nM) was administered with an intravenous injection as described in (Gombash Lampe et al., 2014).

Cell treatment

All drug treatments were done on cortical neurons at DIV4. Neurons were treated for 10h with 10µM MG132 (Sigma, 474790); for 6h with 100nM bafilomycin (Sigma, B1793). Cells were lysed and proteins analyzed by western blot. To evaluate the efficiency of epothilone B to bundle and stabilize microtubules in vitro, neurons were treated for with 10nM epothilone B. AntagomiR-124 (Qiagen, 339132) was delivered via direct uptake (gymnosis) at a concentration

of 100nM in the culture medium.

Immunocytochemistry

Cortical neurons were fixed at DIV4 with Glutaraldehyde (0.5%), Triton-X100 (0.1%) in cytoskeleton buffer (10mM MES, 138mM KCl, 3mM MgCl2, 2mM EGTA, pH 6.1) supplemented with 10% sucrose at 37°C. Glutaraldehyde auto-fluorescence was quenched with 10 min incubation in Sodium Borohydride 1mg/mL. Blocking was performed with PBS-BSA (5%) for 1h at 20°C. Primary antibodies were incubated overnight at 4°C. Secondary fluorochrome-conjugated antibodies were applied 1h30 at 20°C and phalloidin 30min at 20°C. Washes were done in PBS. The following antibodies and reagents were used: rabbit monoclonal anti-NUMA1, diluted 1:200; rat monoclonal anti-tyrosinated TUBULIN antibody (YL1/2), diluted 1:4000; rabbit polyclonal anti-FAT4, diluted 1:100; phalloidin-ATTO488, diluted 1:1000; chicken polyclonal anti-TAU antibody, diluted 1:1000; chicken polyclonal anti-GFP antibody, diluted 1:2000. Secondary antibodies were coupled to Cy2, Cy3 or Cy5 (Jackson Immuno-Research Laboratories).

Permeabilization assay

Cortical neurons were electroporated at DIV0 with 1µg of GFP encoding plasmid and were mixed (1:2) with non-electroporated cells in order to have isolated GFP-positive neurons. At DIV4, cells were treated with BRB80 (80mM PIPES, 1mM EGTA, 1mM MgCl2, pH 6.7) supplemented with Paclitaxel 10µM (Taxol) and Triton-X100 (0.05%), and warmed at 37°C for 3min before fixation. Growth cones were immunostained as described above and all images were acquired with the same parameters and displayed with the same threshold.

Growth cone fractionation

Growth cone and non-growth cone fractions were separated from P0 cortices as in (Leshchyns'ka and Sytnyk, 2013). Briefly, twelve cortices were homogenized by 10 strokes using glass potters, loaded onto a discontinuous 0.75/1.0/2.33M sucrose gradient and spin at 242,000 g for 1h at 4°C in a SW32Ti rotor. Growth cone fractions were collected at the interface load/0.75M sucrose and non-growth cone fractions collected between 0.75/1.0M sucrose and then analyzed by Western Blot.

Mass spectrometry-based quantitative proteomics

Proteins extracted from five biological replicates of growth cones purified from $Hdh^{Q7/Q7}$ and $Hdh^{Q7/Q111}$ mice were solubilized in Laemmli buffer and stacked in the top of a 4-12% NuPAGE gel (Invitrogen). After staining with R-250 Coomassie Blue (Biorad), proteins were digested in-gel using trypsin (modified, sequencing purity, Promega), as previously described (Casabona et al., 2013).

The resulting peptides were analyzed by online nanoliquid chromatography coupled to MS/MS (Ultimate 3000 RSLCnano and Q-Exactive HF, Thermo Fisher Scientific) using a 185 min gradient. For this purpose, the peptides were sampled on a precolumn (300 µm x 5 mm PepMap C18, Thermo Scientific) and separated in a 75 µm x 250 mm C18 column (Reprosil-Pur 120 C18-AQ, 1.9 µm, Dr. Maisch). The MS and MS/MS data were acquired by Xcalibur (Thermo Fisher Scientific).

Peptides and proteins were identified by Mascot (version 2.6.0, Matrix Science) through searches against the i) Uniprot database (*Mus musculus* taxonomy, February 2018 version, https://www.uniprot.org/); ii) a homemade database containing the sequences of classic proteins found in proteomic analyses (human keratins, trypsin, etc.), and iii) the corresponding reversed databases. Trypsin/P was chosen as the enzyme and two missed cleavages were allowed. Precursor and fragment mass error tolerances were set at 10 and 25 milli mass unit, respectively. Peptide modifications allowed during the search were: Carbamidomethyl (C, fixed), Acetyl (Protein N-term, variable) and Oxidation (M, variable). The Proline software (Bouyssie et al., 2020) was used for the compilation, grouping, and filtering of the results (conservation of rank 1 peptides, peptide length ≥ 7 amino acids, peptide score ≥ 25, allowing to reach a false discovery rate of peptide-spectrum-match identifications $< 1\%$ as calculated on peptide-spectrum-match scores by employing the reverse database strategy). Proline was then used to perform a compilation, grouping and MS1 label-free quantification of the identified protein groups. MS data have been deposited to the ProteomeXchange Consortium via the PRIDE partner repository (Perez-Riverol et al., 2019) with the dataset identifier PXD023885.

Statistical analysis was performed using the ProStar software (Wieczorek et al., 2017) on the basis of the quantitative data obtained with the five biological replicates analyzed per genotype. We removed proteins identified in the contaminant database, proteins identified with

fewer than two peptides, proteins identified by MS/MS in fewer than three replicates of one condition, and proteins detected in fewer than four replicates of one condition. After log2 transformation, abundance values were normalized by median centering, before missing value imputation (slsa algorithm for partially observed values in the condition, and DetQuantile algorithm for totally absent values in the condition). Statistical testing was conducted with *limma*, whereby differentially expressed proteins were sorted out using a $\log_2$ (Fold Change) cut-off of 0.67 and a p-value cut-off of 0.01, leading to a FDR inferior to 5% according to the Benjamini-Hochberg estimator.

Microtubule co-sedimentation assay

Polymerization of porcine TUBULIN (T240-A) was performed in BRB80 (80mM PIPES, 1mM EGTA, 1mM MgCl2, pH 6.7) supplemented with GTP (1mM) and glycerol (2.5%) for 1h at 37°C. Paclitaxel 50µM (Taxol) was added for 15min at the end of polymerization. P0-P1 cortices were lysed at 50 µg/µL in BRB80 supplemented with protease and phosphatase inhibitors, then subjected to vortex/ice cycles for 20min. The lysates were cleaned by 245,000g ultracentrifugation for 40 min at 4°C to discard potential polymerized microtubules in the pellet. The supernatant was collected and incubated or not (control) with 2 µM of polymerized microtubules for 30min at RT. The TUBULIN detected by western blot in the control line is the endogenous TUBULIN. Total fraction (input) was collected before ultracentrifugation at 100,000 g for 30min at 23°C in a TLA100.3 rotors. Supernatant was discarded and pellet fractions were obtained by re-suspending pellet in a volume equal to the initial volume. 20µl of each fraction were loaded onto the gel for western blot analysis.

Nuclear and cytoplasmic proteins extraction

P0 cortices were harvested in cytoplasmic protein low-salt extraction buffer (10 mM HEPES pH 7.9, 10 mM KCl, 0.1 mM EDTA, 1 mM DTT, 0.5 mM PMSF, 0.6 % Nonidet P-40 supplemented with 1/100 protease and phosphatases inhibitors, Sigma-Aldrich, P8340 and P5726). The cortices were homogenized by pipetting up and down approximately 10 times with a P1000 Gilson. After 15min on ice, the cytosolic fraction was collected after centrifugation at 10,000 rpm for 10min at 4°C. The pellet was washed 4 times with cold PBS. The nuclear proteins were extracted from resuspension of the pellet with RIPA buffer (150mM NaCl, 1%

Nonidet P-40, 0.5% sodium deoxycholate, 0.1% SDS, 50mM tris HCl pH8.0 supplemented with 1/100 protease and phosphatases inhibitors, Sigma-Aldrich P8340 and P5726). The suspension was briefly sonicated to homogenize the lysate. After 15 min on ice, the samples were centrifuged at 16,000 g for 15min at 4°C and the supernatant (nuclear fraction) was collected.

Western blot

Cortical neurons were harvested in protein extraction buffer (20mM Tris-HCl pH7.4, 137mM NaCl, 2mM EDTA, 1% Triton X-100 supplemented with 1/100 protease and phosphatases inhibitors, Sigma-Aldrich, P8340 and P5726) and frozen at 80°C until protein extraction. Protein extraction of neurons was performed by pipetting up and down approximately 10 times with a P1000 Gilson. The supernatants were collected after centrifugation at 10,000rpm for 10 min at 4°C. Protein concentration was measured by the BCA method. Proteins were treated with SDS-PAGE sample buffer [6X concentrated: 350mM Tris 10% (w/v), SDS 30% (v/v) in glycerol, 0.6M DTT, 0.06% (w/v) bromophenol blue], boiled 5min at 95°C, and loaded on 8%. Polyacrylamide gel.

Proteins were transferred onto PVDF (polyvinylidine difluoride) membranes, blocked with 5% bovine serum albumin and 0.5% Tween (Euromedex) in TBS (TBST) for 1h at room temperature, and probed overnight at 4°C with the following primary antibodies diluted in 5% bovine serum albumin TBST: 1:1000 rabbit anti-NUMA1 (ab109262, Abcam), 1:2000 rabbit anti-VINCULIN (V9131, Sigma), 1:250 mouse anti-GM130 (610822, BD transduction), 1:500 mouse anti-JIP1 (B-7, sc-25267 Santa Cruz Biotechnology), 1:5000 mouse anti-αTUBULIN (T9026, Sigma), 1:1000 rabbit anti-LAMIN B1 (ab133741, abcam), 1:1000 mouse anti-poly-UBIQUITIN antibody (Clinisciences, LS-C107107-25), 1:500 rabbit anti-p62 (Sigma, P0067). Washes were performed with TBS-Tween (0.1%). HRP-conjugated antibodies were incubated for 1h at room temperature and membranes were revealed by using ECL reagent (ThermoFisher Scientific) with a Chemidoc imaging device (Biorad).

Quantitative real-time PCR

For NUMA1 mRNA analysis, total RNA was extracted from P0 cortices using the NucleoSpin RNA extraction kit (Macherey-Nagel, 740955). RNA samples were retrotranscribed with the iScript Ready-to-Use cDNA supermix (Biorad, 1708840). One microgram of cDNA was

submitted to qPCR using the SsoAdvanced SYBR Green supermix (Biorad, 1725272) with a specific pair of primers for NUMA1 (Gene Globe ID QT00109557, Qiagen). CycloG (5′-AAGAATCGTCGCTGGTATG-3′, 5′-AAAGCCGATGACAAGGAG-3′), MTBP (5′-GGGGTCATAGGAGTCATTGG-3′, 5′-ACATCTCAGCAACCCACACA-3′), and PGK1 (5'-TAGTGGCTGAGATGTGGCACAG-3', 5'- GCTCACTTCCTTTCTCAGGCAG-3') genes were used as internal controls. Fold changes were calculated using the 2-ΔΔCt method. Data were analyzed from six independent experiments and presented as the mean ± SEM.

For miRNA quantification, RNA was extracted from P0 cortices using the miRNeasy Tissue/Cells Advanced Mini Kit (Qiagen, 217604). Of the extracted RNA, 10 ng was used for reverse transcription following the manufacturer's instructions using miRCURY LNA RT Kit (Qiagen, 339340). qPCR reactions were performed following manufacturer's instructions for miRCURY LNA SYBR Green PCR Kit (Qiagen, 339345) with a specific pair of primers for mmu-miR-124-3p (Qiagen, MIMAT0000134-YP00206026); mmu-miR-148b-3p (Qiagen, MIMAT0000580-YP00204047); mmu-miR-130b-3p (Quiagen, MIMAT0000387-YP00204317); mmu-miR-7a-1-3p (Qiagen, MIMAT0004670-YP00205888); mmu-miR-31-5p (Qiagen, MIMAT0000538-YP00205159); mmu-miR-22-3p (Qiagen, MIMAT0000531-YP00204606); mmu-miR-152-3p (Qiagen, MIMAT0000162-YP00204294); mmu-miR-125b-5p (Qiagen, MIMAT0000423-YP00205713); mmu-miR-351-5p (Qiagen, MIMAT0000609-YP00205011); mmu-miR-301a-3p (Qiagen, MIMAT0000688-YP00205601) and U6 snRNA (hsa, mmu) (Qiagen, YP00203907) was used as internal control. miRNAs changes were quantified with the 2−ΔΔCT method using RNU6–1 (RNA, U6 small nuclear 1) as control.

Plasmid constructs

To delete the NLS region in the pCDH-Ubc-NUMA1FL and pCDH-Ubc-NuMA1deltaMBD constructs (Gallini *et al.*, 2016), we performed an inverse PCR with the following oligos: Delta NLS sense 5'-TCACCACCGTGTCCCTGGAACCTCATCAGG-3';
Delta NLS anti-sense 5'-GGGACACGGTGGTGATACCGGTGCC-3'. Subsequently both constructs were sub cloned into a pCAG-GFP vector (addgene 11150) using Pro Ligation-Free Cloning Kit from (abm E086/E087). BsrGI was used as restriction site. For the lox-STOP-lox-GFPshNUMA1 constructs, we used a pCALNL-GFP-hU6 plasmid into which we cloned the shNUMA1. To build the pCALNL-GFP-hU6 the humanU6 promoter has been PCR amplified

from the pLKO.1 (addgene 10878) and cloned into the pCALNL-GFP plasmid (addgene, 13770) into the XbaI unique restriction site using Pro Ligation-Free Cloning Kit (abm E086/E087). shNUMA1 was introduced in the AgeI unique restriction site of this resulting vector, annealing the 2 following oligos: sens (targeted sequence is in bold) 5'gatttaaattgaattccgg**ccttagtctctggacctagaa**ctcgag**ttctaggtccagagactaagg**tttttggggatccccggtcgccaccatg3'; anti-sense (targeted sequence is in bold) 5'catggtggcgaccggggatccccaaaaa**ccttagtctctggacctagaa**ctcgag**ttctaggtccagagactaagg**ccggaattcaatttaaatc-3'. All constructs were sequenced (GENEWIZ).

Image acquisition

For the in vitro axonal tracking, cortical neurons were imaged with Axio Scan.Z1 slide scanner (Colibri.7; 20X objective; Zeiss). The brain sections for in vivo axonal track were acquired using an inverted confocal microscopy (LSM710, Zeiss). High-resolution images on growth cones were acquired using an inverted confocal microscope (LSM710, Zeiss) with Airyscan detector and a 63 objective (1.4 NA, Zeiss).

QUANTIFICATION AND STATISTICAL ANALYSIS

Data analysis

All the data were analyzed using NIH ImageJ (http://rsbweb. nih.gov/ij/). For axonal tracking in cell culture, the axon was defined as the longest neurite measuring at least 100µm, using the ImageJ segmented line tool. Measurements were taken from the neck of the axon at the base of the soma to the growth cone. For axon branching in cell culture, we considered an extension of at least 15µm to constitute a branch. On brain sections, axon tracts were traced using the edge of the mem-RFP labeled region as the starting point.

In P21 mice, we analyzed 4 different regions of interest (1 to 4, Figure 1C). For region 1 in the ipsilateral cortex, we measured the mean in layer V after subtracting the mean intensity background from a cortical region presenting no specific staining. Region 2 was traced in the contralateral somatosensory cortex, where the branching was at its maximum for both genotypes; we measured the mean in layers V, II/III, and white matter (WM) V after subtracting the mean intensity background from a cortical region with no specific staining. Region 3 represents a line

scan of 200-pixel width drown across the middle region of corpus callosum. Finally, region 4 represents a line scan of 200-pixel width drawn in layer II/III all along the contralateral cortex from the parietal to the auditory region, where the last branching point was present in the control condition. Growth cone areas were measured from the axon shaft up to the tips of filopodia, defined by phalloidin staining. Exploratory microtubules were measured from their tips to the main microtubule bundle. To assess the microtubule bundling state, we plotted the maximum value obtained after measuring the mean fluorescence intensity of Tyr- TUBULIN staining along a line scan width of 60 pixels.

Statistical analyses

GraphPad Prism 6.0 software (San Diego, CA) was used for statistical analyses. Outliers were identified applying the Rout method. Sample sizes were chosen based on similar experiments in the references to ensure statistically significant results while minimizing the number of animals used. Significance was assessed using a two-tailed Student's t test or Mann-Whitney U test, depending on the normality test (Shapiro-Wilk normality test or Kolmogorov-Smirnov test). The samples following a Gaussian distribution were expressed as mean ± SEM. Data without a normal distribution were displayed as box-whisker plots representing the 25th, 50th and 75th percentiles.

REFERENCES

Al-Ramahi, I., Lu, B., Di Paola, S., Pang, K., de Haro, M., Peluso, I., Gallego-Flores, T., Malik, N.T., Erikson, K., Bleiberg, B.A., et al. (2018). High-Throughput Functional Analysis Distinguishes Pathogenic, Nonpathogenic, and Compensatory Transcriptional Changes in Neurodegeneration. Cell Syst *7*, 28-40 e24. 10.1016/j.cels.2018.05.010.

Alcamo, E.A., Chirivella, L., Dautzenberg, M., Dobreva, G., Farinas, I., Grosschedl, R., and McConnell, S.K. (2008). Satb2 regulates callosal projection neuron identity in the developing cerebral cortex. Neuron *57*, 364-377. 10.1016/j.neuron.2007.12.012.

Barnat, M., Capizzi, M., Aparicio, E., Boluda, S., Wennagel, D., Kacher, R., Kassem, R., Lenoir, S., Agasse, F., Braz, B., et al. (2020). Huntington disease alters human neurodevelopment. Science *369*, 787-793.

Barnat, M., Le Friec, J., Benstaali, C., and Humbert, S. (2017). Huntingtin-mediated multipolar-bipolar transition of newborn cortical neurons is critical for their postnatal neuronal morphology. Neuron *93*, 99-114. 10.1016/j.neuron.2016.11.035.

Bouyssie, D., Hesse, A.M., Mouton-Barbosa, E., Rompais, M., Macron, C., Carapito, C., Gonzalez de Peredo, A., Coute, Y., Dupierris, V., Burel, A., et al. (2020). Proline: an efficient and user-friendly software suite for large-scale proteomics. Bioinformatics *36*, 3148-3155. 10.1093/bioinformatics/btaa118.

Casabona, M.G., Vandenbrouck, Y., Attree, I., and Coute, Y. (2013). Proteomic characterization of Pseudomonas aeruginosa PAO1 inner membrane. Proteomics *13*, 2419-2423. 10.1002/pmic.201200565.

Casella, C., Lipp, I., Rosser, A., Jones, D.K., and Metzler-Baddeley, C. (2020). A Critical Review of White Matter Changes in Huntington's Disease. Mov Disord *35*, 1302-1311. 10.1002/mds.28109.

Cepeda, C., Hurst, R.S., Calvert, C.R., Hernandez-Echeagaray, E., Nguyen, O.K., Jocoy, E., Christian, L.J., Ariano, M.A., and Levine, M.S. (2003). Transient and progressive electrophysiological alterations in the corticostriatal pathway in a mouse model of Huntington's disease. J Neurosci *23*, 961-969.

Consortium, H.D.i. (2017). Developmental alterations in Huntington's disease neural cells and pharmacological rescue in cells and mice. Nat Neurosci *20*, 648-660. 10.1038/nn.4532.

Dajas-Bailador, F., Jones, E.V., and Whitmarsh, A.J. (2008). The JIP1 scaffold protein regulates axonal development in cortical neurons. Curr Biol *18*, 221-226. 10.1016/j.cub.2008.01.025.

Dent, E.W., Gupton, S.L., and Gertler, F.B. (2011). The growth cone cytoskeleton in axon outgrowth and guidance. Cold Spring Harb Perspect Biol *3*. 10.1101/cshperspect.a001800.

di Pietro, F., Echard, A., and Morin, X. (2016). Regulation of mitotic spindle orientation: an integrated view. EMBO Rep *17*, 1106-1130. 10.15252/embr.201642292.

Eshraghi, M., Karunadharma, P.P., Blin, J., Shahani, N., Ricci, E.P., Michel, A., Urban, N.T., Galli, N., Sharma, M., Ramirez-Jarquin, U.N., et al. (2021). Mutant Huntingtin stalls ribosomes and represses protein synthesis in a cellular model of Huntington disease. Nat Commun *12*, 1461. 10.1038/s41467-021-21637-y.

Estevez-Fraga, C., Scahill, R., Rees, G., Tabrizi, S.J., and Gregory, S. (2020). Diffusion imaging in Huntington's disease: comprehensive review. J Neurol Neurosurg Psychiatry. 10.1136/jnnp-2020-324377.

Fame, R.M., MacDonald, J.L., and Macklis, J.D. (2011). Development, specification, and diversity of callosal projection neurons. Trends Neurosci *34*, 41-50. 10.1016/j.tins.2010.10.002.

Ferhat, L., Cook, C., Kuriyama, R., and Baas, P.W. (1998). The nuclear/mitotic apparatus protein NuMA is a component of the somatodendritic microtubule arrays of the neuron. J Neurocytol *27*, 887-899. 10.1023/a:1006949006728.

Forth, S., Hsia, K.C., Shimamoto, Y., and Kapoor, T.M. (2014). Asymmetric friction of nonmotor MAPs can lead to their directional motion in active microtubule networks. Cell *157*, 420-432. 10.1016/j.cell.2014.02.018.

Gallini, S., Carminati, M., De Mattia, F., Pirovano, L., Martini, E., Oldani, A., Asteriti, I.A., Guarguaglini, G., and Mapelli, M. (2016). NuMA Phosphorylation by Aurora-A Orchestrates Spindle Orientation. Curr Biol *26*, 458-469. 10.1016/j.cub.2015.12.051.

Godin, J.D., Colombo, K., Molina-Calavita, M., Keryer, G., Zala, D., Charrin, B.C., Dietrich, P., Volvert, M.L., Guillemot, F., Dragatsis, I., et al. (2010). Huntingtin is required for mitotic spindle orientation and mammalian neurogenesis. Neuron *67*, 392-406. 10.1016/j.neuron.2010.06.027.

Gombash Lampe, S.E., Kaspar, B.K., and Foust, K.D. (2014). Intravenous injections in neonatal mice. J Vis Exp, e52037. 10.3791/52037.

Hand, R.A., Khalid, S., Tam, E., and Kolodkin, A.L. (2015). Axon Dynamics during Neocortical Laminar Innervation. Cell Rep *12*, 172-182. 10.1016/j.celrep.2015.06.026.

Haren, L., and Merdes, A. (2002). Direct binding of NuMA to tubulin is mediated by a novel sequence motif in the tail domain that bundles and stabilizes microtubules. J Cell Sci *115*, 1815-1824.

Hedreen, J.C., Peyser, C.E., Folstein, S.E., and Ross, C.A. (1991). Neuronal loss in layers V and VI of cerebral cortex in Huntington's disease. Neurosci Lett *133*, 257-261.

Igarashi, M. (2014). Proteomic identification of the molecular basis of mammalian CNS growth cones. Neurosci Res *88*, 1-15. 10.1016/j.neures.2014.07.005.

Ilieva, M., Nielsen, T.T., Michel, T., and Pankratova, S. (2019). FGF2 and dual agonist of NCAM and FGF receptor 1, Enreptin, rescue neurite outgrowth loss in hippocampal neurons expressing mutated huntingtin proteins. J Neural Transm (Vienna) *126*, 1493-1500. 10.1007/s00702-019-02073-1.

Jayaraman, S., Chittiboyina, S., Bai, Y., Abad, P.C., Vidi, P.A., Stauffacher, C.V., and Lelievre, S.A. (2017). The nuclear mitotic apparatus protein NuMA controls rDNA transcription and mediates the nucleolar stress response in a p53-independent manner. Nucleic Acids Res *45*, 11725-11742. 10.1093/nar/gkx782.

Ji, S.J., and Jaffrey, S.R. (2014). Axonal transcription factors: novel regulators of growth cone-to-nucleus signaling. Dev Neurobiol *74*, 245-258. 10.1002/dneu.22112.

Jin, M., Pomp, O., Shinoda, T., Toba, S., Torisawa, T., Furuta, K., Oiwa, K., Yasunaga, T., Kitagawa, D., Matsumura, S., et al. (2017). Katanin p80, NuMA and cytoplasmic dynein cooperate to control microtubule dynamics. Sci Rep *7*, 39902. 10.1038/srep39902.

Kugler, C., Thielscher, C., Tambe, B.A., Schwarz, M.K., Halle, A., Bradke, F., and Petzold, G.C. (2020). Epothilones Improve Axonal Growth and Motor Outcomes after Stroke in the Adult Mammalian CNS. Cell Rep Med *1*, 100159. 10.1016/j.xcrm.2020.100159.

Leshchyns'ka, I., and Sytnyk, V. (2013). Isolation of Growth Cones from Mouse Brain. Bio-protocol *3*, e853. 10.21769/BioProtoc.853.

Lewis, T.L., Jr., Courchet, J., and Polleux, F. (2013). Cell biology in neuroscience: Cellular and molecular mechanisms underlying axon formation, growth, and branching. J Cell Biol *202*, 837-848. 10.1083/jcb.201305098.

Mangin, J.F., Riviere, D., Duchesnay, E., Cointepas, Y., Gaura, V., Verny, C., Damier, P., Krystkowiak, P., Bachoud-Levi, A.C., Hantraye, P., et al. (2020). Neocortical morphometry in Huntington's disease: Indication of the coexistence of abnormal neurodevelopmental and neurodegenerative processes. Neuroimage Clin *26*, 102211. 10.1016/j.nicl.2020.102211.

McCormick, L.E., and Gupton, S.L. (2020). Mechanistic advances in axon pathfinding. Curr Opin Cell Biol *63*, 11-19. 10.1016/j.ceb.2019.12.003.

McKinstry, S.U., Karadeniz, Y.B., Worthington, A.K., Hayrapetyan, V.Y., Ozlu, M.I., Serafin-Molina, K., Risher, W.C., Ustunkaya, T., Dragatsis, I., Zeitlin, S., et al. (2014). Huntingtin is required for normal excitatory synapse development in cortical and striatal circuits. J Neurosci *34*, 9455-9472. 10.1523/JNEUROSCI.4699-13.2014.

Mehta, S.R., Tom, C.M., Wang, Y., Bresee, C., Rushton, D., Mathkar, P.P., Tang, J., and Mattis, V.B. (2018). Human Huntington's Disease iPSC-Derived Cortical Neurons Display Altered Transcriptomics, Morphology, and Maturation. Cell Rep *25*, 1081-1096 e1086. 10.1016/j.celrep.2018.09.076.

Menalled, L.B., Kudwa, A.E., Miller, S., Fitzpatrick, J., Watson-Johnson, J., Keating, N., Ruiz, M., Mushlin, R., Alosio, W., McConnell, K., et al. (2012). Comprehensive behavioral and molecular characterization of a new knock-in mouse model of Huntington's disease: zQ175. PLoS One *7*, e49838. 10.1371/journal.pone.0049838.

Merdes, A., Ramyar, K., Vechio, J.D., and Cleveland, D.W. (1996). A complex of NuMA and cytoplasmic dynein is essential for mitotic spindle assembly. Cell *87*, 447-458.

Molero, A.E., Arteaga-Bracho, E.E., Chen, C.H., Gulinello, M., Winchester, M.L., Pichamoorthy, N., Gokhan, S., Khodakhah, K., and Mehler, M.F. (2016). Selective expression of mutant huntingtin during development recapitulates characteristic features of Huntington's disease. Proc Natl Acad Sci U S A *116*, 5736-5741. 10.1073/pnas.1603871113.

Molina-Calavita, M., Barnat, M., Elias, S., Aparicio, E., Piel, M., and Humbert, S. (2014). Mutant huntingtin affects cortical progenitor cell division and development of the mouse neocortex. J Neurosci *34*, 10034-10040. 10.1523/JNEUROSCI.0715-14.2014.

Nopoulos, P.C., Aylward, E.H., Ross, C.A., Mills, J.A., Langbehn, D.R., Johnson, H.J., Magnotta, V.A., Pierson, R.K., Beglinger, L.J., Nance, M.A., et al. (2011). Smaller intracranial volume in prodromal Huntington's disease: evidence for abnormal neurodevelopment. Brain *134*, 137-142. 10.1093/brain/awq280.

Pasterkamp, R.J., and Burk, K. (2020). Axon guidance receptors: Endocytosis, trafficking and downstream signaling from endosomes. Prog Neurobiol, 101916. 10.1016/j.pneurobio.2020.101916.

Perez-Riverol, Y., Csordas, A., Bai, J., Bernal-Llinares, M., Hewapathirana, S., Kundu, D.J., Inuganti, A., Griss, J., Mayer, G., Eisenacher, M., et al. (2019). The PRIDE database and related tools and resources in 2019: improving support for quantification data. Nucleic Acids Res *47*, D442-D450. 10.1093/nar/gky1106.

Pinto-Costa, R., and Sousa, M.M. (2021). Microtubules, actin and cytolinkers: how to connect cytoskeletons in the neuronal growth cone. Neurosci Lett *747*, 135693. 10.1016/j.neulet.2021.135693.

Reis, S.A., Thompson, M.N., Lee, J.M., Fossale, E., Kim, H.H., Liao, J.K., Moskowitz, M.A., Shaw, S.Y., Dong, L., Haggarty, S.J., et al. (2011). Striatal neurons expressing full-length mutant huntingtin exhibit decreased N-cadherin and altered neuritogenesis. Hum Mol Genet *20*, 2344-2355. 10.1093/hmg/ddr127.

Ren, Y., and Suter, D.M. (2016). Increase in Growth Cone Size Correlates with Decrease in Neurite Growth Rate. Neural Plast *2016*, 3497901. 10.1155/2016/3497901.

Rub, U., Seidel, K., Heinsen, H., Vonsattel, J.P., den Dunnen, W.F., and Korf, H.W. (2016). Huntington's disease (HD): the neuropathology of a multisystem neurodegenerative disorder of the human brain. Brain Pathol *26*, 726-740. 10.1111/bpa.12426.

Ruschel, J., Hellal, F., Flynn, K.C., Dupraz, S., Elliott, D.A., Tedeschi, A., Bates, M., Sliwinski, C., Brook, G., Dobrindt, K., et al. (2015). Axonal regeneration. Systemic administration of epothilone B promotes axon regeneration after spinal cord injury. Science *348*, 347-352. 10.1126/science.aaa2958.

Saudou, F., and Humbert, S. (2016). The Biology of Huntingtin. Neuron *89*, 910-926. 10.1016/j.neuron.2016.02.003.

Scahill, R.I., Zeun, P., Osborne-Crowley, K., Johnson, E.B., Gregory, S., Parker, C., Lowe, J., Nair, A., O'Callaghan, C., Langley, C., et al. (2020). Biological and clinical characteristics of gene carriers far from predicted onset in the Huntington's disease Young Adult Study (HD-YAS): a cross-sectional analysis. Lancet Neurol *19*, 502-512. 10.1016/S1474-4422(20)30143-5.

Suzuki, N., Akiyama, T., Warita, H., and Aoki, M. (2020). Omics Approach to Axonal Dysfunction of Motor Neurons in Amyotrophic Lateral Sclerosis (ALS). Front Neurosci *14*, 194. 10.3389/fnins.2020.00194.

Tang, C.C., Feigin, A., Ma, Y., Habeck, C., Paulsen, J.S., Leenders, K.L., Teune, L.K., van Oostrom, J.C., Guttman, M., Dhawan, V., and Eidelberg, D. (2013). Metabolic network as a progression biomarker of premanifest Huntington's disease. J Clin Invest *123*, 4076-4088. 10.1172/JCI69411.

Tereshchenko, A.V., Schultz, J.L., Bruss, J.E., Magnotta, V.A., Epping, E.A., and Nopoulos, P.C. (2020). Abnormal development of cerebellar-striatal circuitry in Huntington disease. Neurology *9*, 551-557. 10.1212/WNL.0000000000009364.

Tong, Y., Ha, T.J., Liu, L., Nishimoto, A., Reiner, A., and Goldowitz, D. (2011). Spatial and temporal requirements for huntingtin (Htt) in neuronal migration and survival during brain development. J Neurosci *31*, 14794-14799. 31/41/14794 [pii]

10.1523/JNEUROSCI.2774-11.2011.

Torii, T., Ogawa, Y., Liu, C.H., Ho, T.S., Hamdan, H., Wang, C.C., Oses-Prieto, J.A., Burlingame, A.L., and Rasband, M.N. (2020). NuMA1 promotes axon initial segment assembly through inhibition of endocytosis. J Cell Biol *219*. 10.1083/jcb.201907048.

Virlogeux, A., Moutaux, E., Christaller, W., Genoux, A., Bruyere, J., Fino, E., Charlot, B., Cazorla, M., and Saudou, F. (2018). Reconstituting corticostriatal network on-a-chip reveals the contribution of the presynaptic compartment to Huntington's Disease. Cell Rep *22*, 110-122. 10.1016/j.celrep.2017.12.013.

Wang, N., Gray, M., Lu, X.H., Cantle, J.P., Holley, S.M., Greiner, E., Gu, X., Shirasaki, D., Cepeda, C., Li, Y., et al. (2014). Neuronal targets for reducing mutant huntingtin expression to ameliorate disease in a mouse model of Huntington's disease. Nat Med *20*, 536-541. 10.1038/nm.3514.

Wheeler, V.C., Gutekunst, C.A., Vrbanac, V., Lebel, L.A., Schilling, G., Hersch, S., Friedlander, R.M., Gusella, J.F., Vonsattel, J.P., Borchelt, D.R., and MacDonald, M.E. (2002). Early phenotypes that presage late-onset neurodegenerative disease allow testing of modifiers in Hdh CAG knock-in mice. Hum Mol Genet *11*, 633-640.

Wieczorek, S., Combes, F., Lazar, C., Giai Gianetto, Q., Gatto, L., Dorffer, A., Hesse, A.M., Coute, Y., Ferro, M., Bruley, C., and Burger, T. (2017). DAPAR & ProStaR: software to perform statistical analyses in quantitative discovery proteomics. Bioinformatics *33*, 135-136. 10.1093/bioinformatics/btw580.

Wilson, C., and Caceres, A. (2020). New insights on epigenetic mechanisms supporting axonal development: histone marks and miRNAs. FEBS J. 10.1111/febs.15673.

Zhao, X., Chen, X.Q., Han, E., Hu, Y., Paik, P., Ding, Z., Overman, J., Lau, A.L., Shahmoradian, S.H., Chiu, W., et al. (2016). TRiC subunits enhance BDNF axonal transport and rescue striatal atrophy in Huntington's disease. Proc Natl Acad Sci U S A *113*, E5655-5664. 10.1073/pnas.1603020113.

FIGURE 1

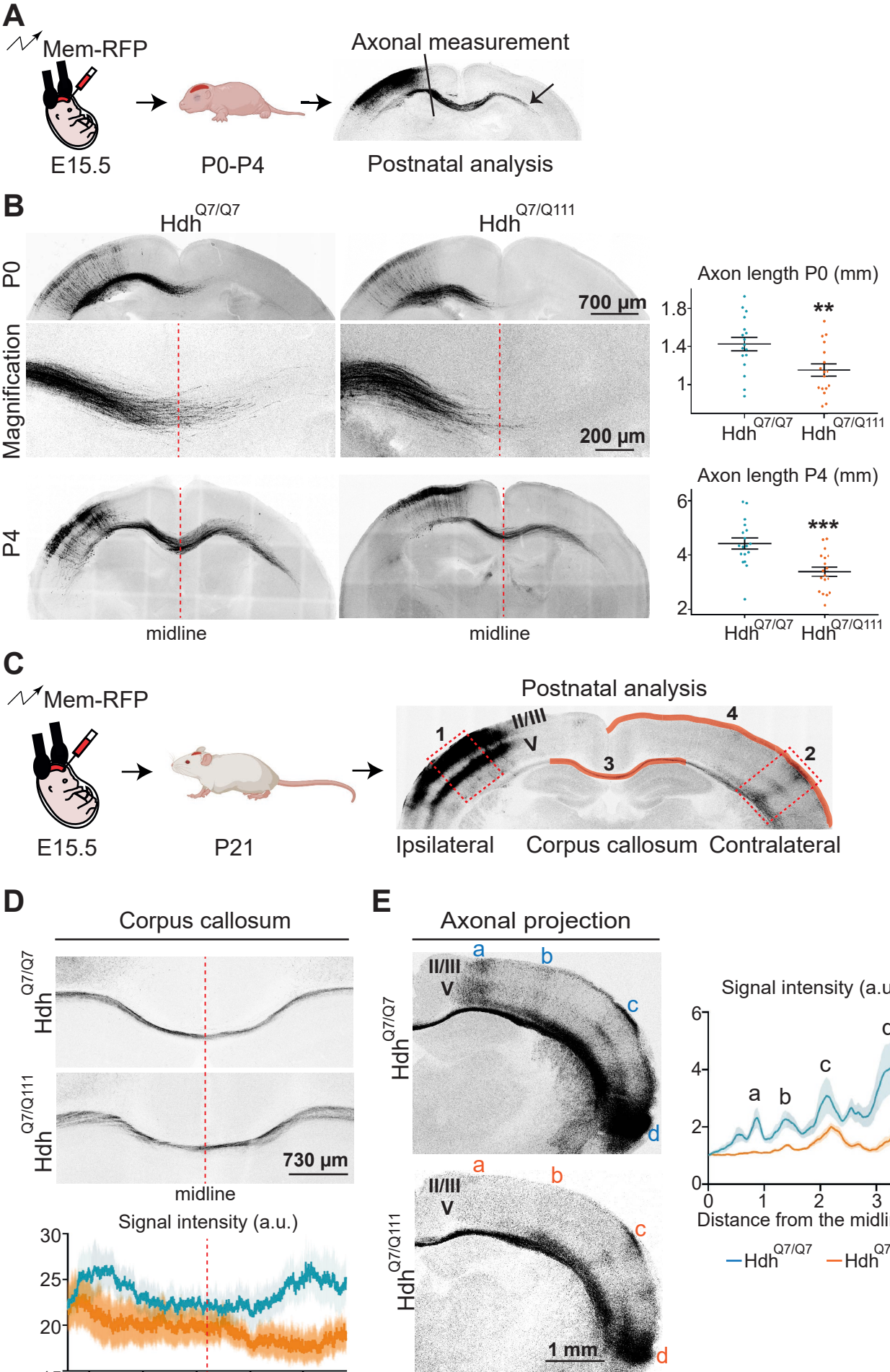
A
Mem-RFP
E15.5
P0-P4
Axonal measurement
Postnatal analysis
B
Hdh Q7/Q7
Hdh Q7/Q111
P0
Magnification
P4
700 µm
200 µm
midline
midline
Axon length P0 (mm)
Axon length P4 (mm)
**
***
C
Mem-RFP
E15.5
P21
Postnatal analysis
I/III
V
1
2
3
4
Ipsilateral
Corpus callosum
Contralateral
D
Corpus callosum
Hdh Q7/Q7
Hdh Q7/Q111
730 µm
midline
Signal intensity (a.u.)
Distance from the injection point (mm)
E
Axonal projection
a
b
c
d
1 mm
Signal intensity (a.u.)
Distance from the midline (mm)

FIGURE 2

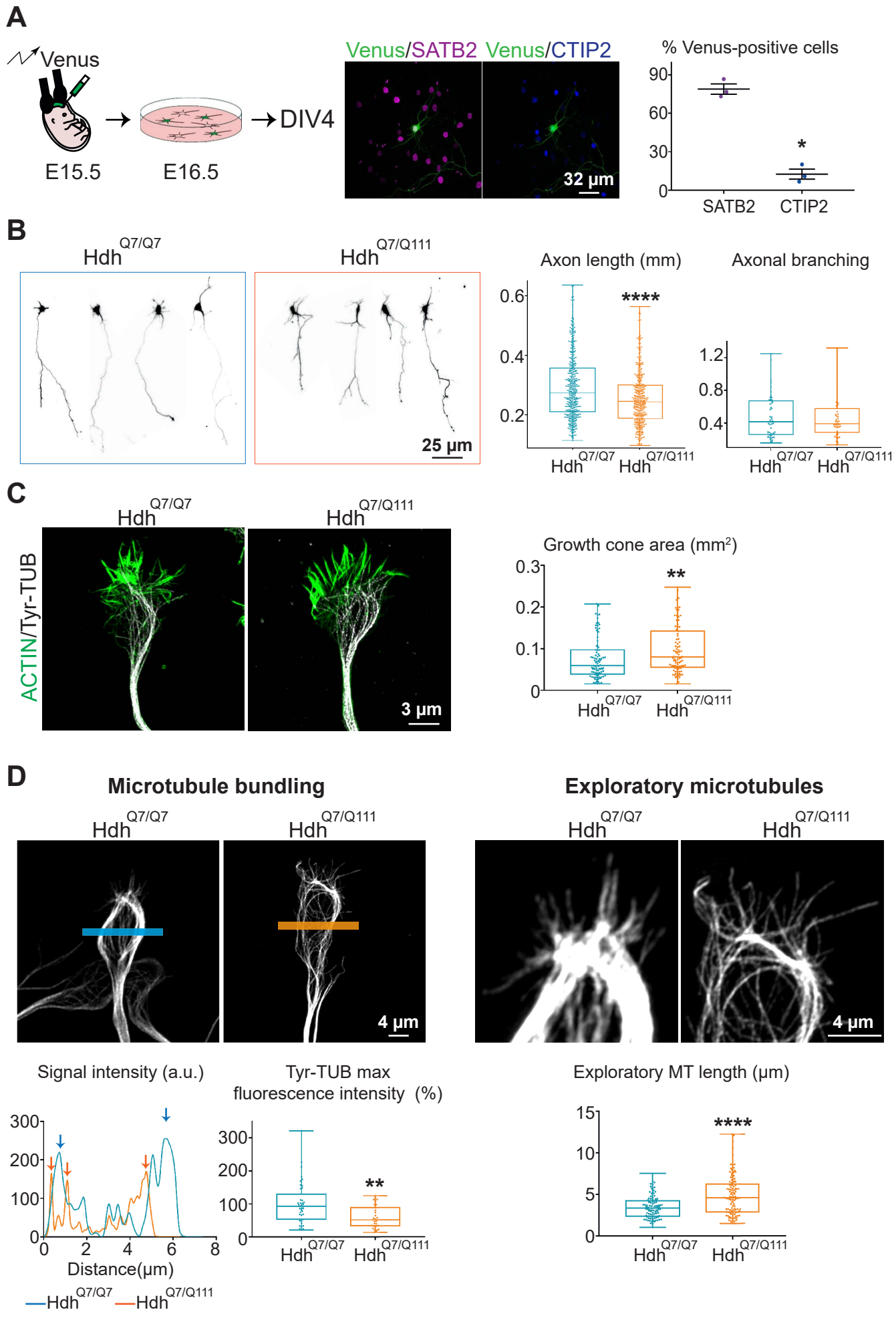
A
Venus
E15.5
E16.5
DIV4
Venus/SATB2 Venus/CTIP2
32 µm
% Venus-positive cells
SATB2
CTIP2
B
Hdh Q7/Q7
Hdh Q7/Q111
25 µm
Axon length (mm)
Axonal branching
****
C
ACTIN/Tyr-TUB
3 µm
Growth cone area (mm²)
**
D
Microtubule bundling
Exploratory microtubules
4 µm
Signal intensity (a.u.)
Distance(µm)
Tyr-TUB max fluorescence intensity (%)
Exploratory MT length (µm)

FIGURE 3

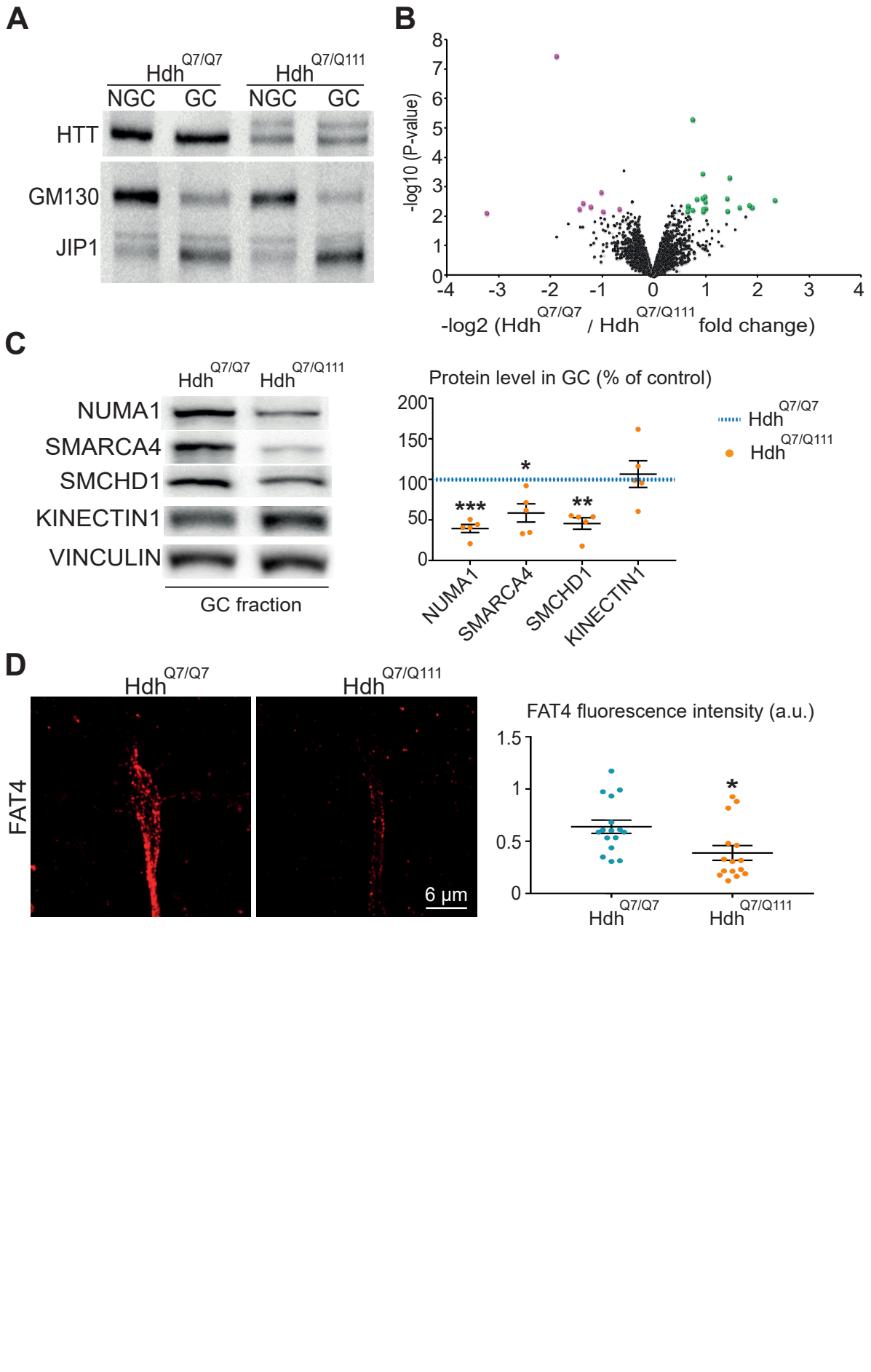
A
Hdh Q7/Q7
Hdh Q7/Q111
NGC GC NGC GC
HTT
GM130
JIP1
B
-log10 (P-value)
-log2 (Hdh Q7/Q7 / Hdh Q7/Q111 fold change)
C
Hdh Q7/Q7
Hdh Q7/Q111
NUMA1
SMARCA4
SMCHD1
KINECTIN1
VINCULIN
GC fraction
Protein level in GC (% of control)
Hdh Q7/Q7
Hdh Q7/Q111
NUMA1
SMARCA4
SMCHD1
KINECTIN1
D
Hdh Q7/Q7
Hdh Q7/Q111
FAT4
6 µm
FAT4 fluorescence intensity (a.u.)
Hdh Q7/Q7
Hdh Q7/Q111

FIGURE 4

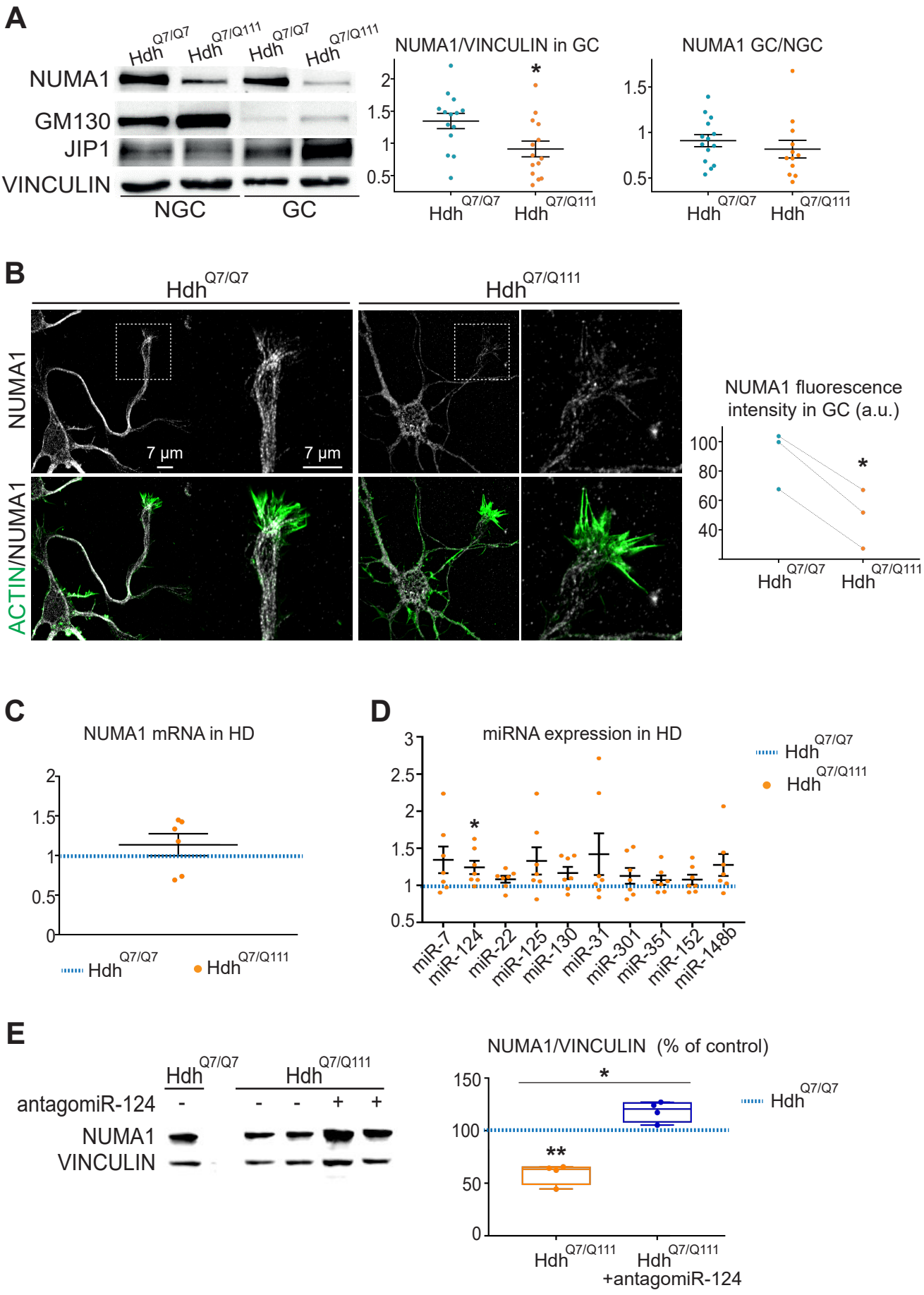
A
Hdh Q7/Q7
Hdh Q7/Q111
Hdh Q7/Q7
Hdh Q7/Q111
NUMA1
GM130
JIP1
VINCULIN
NGC
GC
NUMA1/VINCULIN in GC
NUMA1 GC/NGC
B
Hdh Q7/Q7
Hdh Q7/Q111
NUMA1
ACTIN/NUMA1
7 µm
7 µm
NUMA1 fluorescence intensity in GC (a.u.)
C
NUMA1 mRNA in HD
D
miRNA expression in HD
miR-7
miR-124
miR-22
miR-125
miR-130
miR-31
miR-301
miR-351
miR-152
miR-148b
E
antagomiR-124
NUMA1
VINCULIN
NUMA1/VINCULIN (% of control)
Hdh Q7/Q111 +antagomiR-124

FIGURE 5

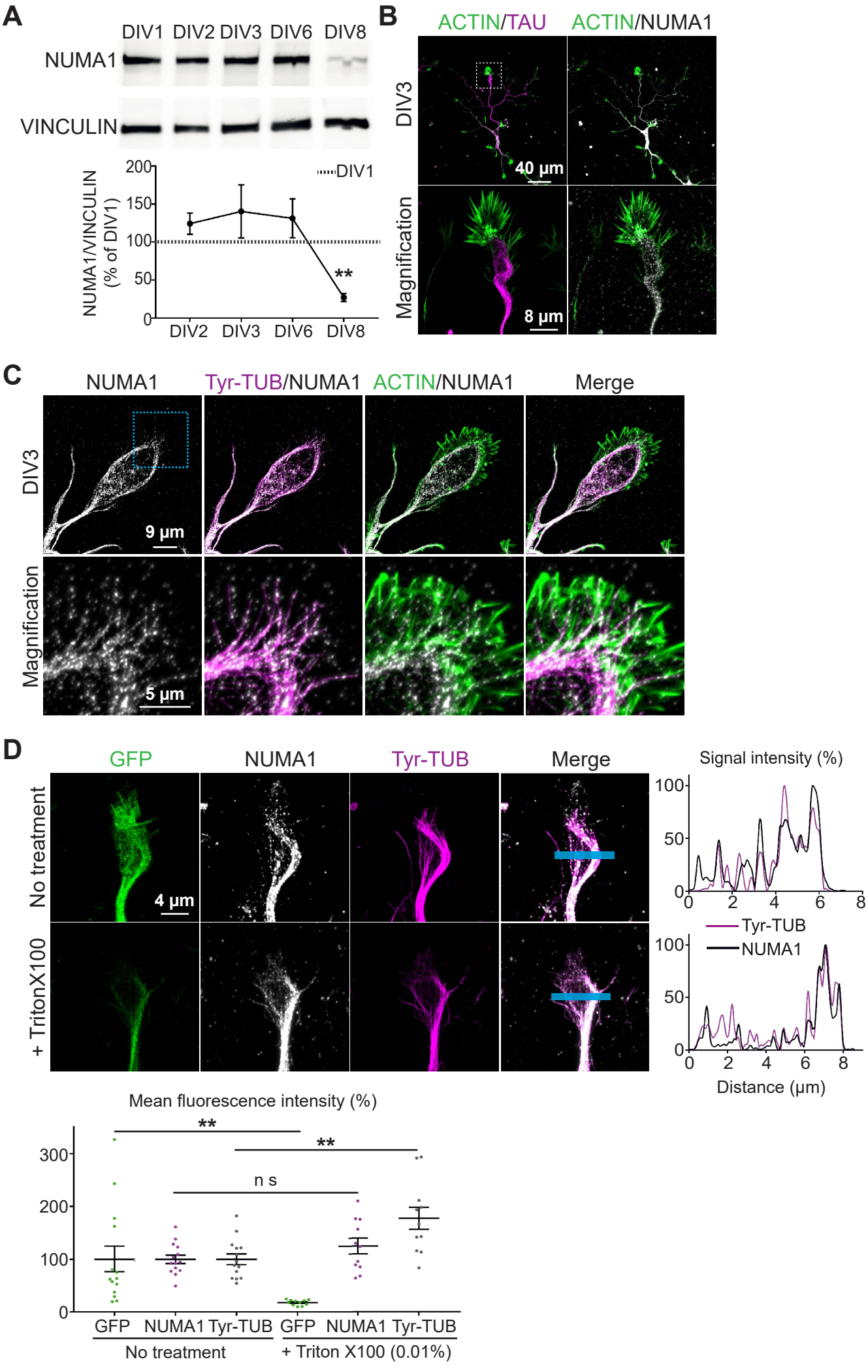
A
DIV1 DIV2 DIV3 DIV6 DIV8
NUMA1
VINCULIN
NUMA1/VINCULIN (% of DIV1)
200
150
100
50
0
DIV1
**
DIV2 DIV3 DIV6 DIV8
B
ACTIN/TAU
ACTIN/NUMA1
DIV3
40 µm
Magnification
8 µm
C
NUMA1
Tyr-TUB/NUMA1
ACTIN/NUMA1
Merge
DIV3
9 µm
Magnification
5 µm
D
GFP
NUMA1
Tyr-TUB
Merge
No treatment
+ TritonX100
4 µm
Signal intensity (%)
100
50
0
0 2 4 6 8
Tyr-TUB
NUMA1
Distance (µm)
Mean fluorescence intensity (%)
300
200
100
0
**
**
n s
GFP NUMA1 Tyr-TUB GFP NUMA1 Tyr-TUB
No treatment
+ Triton X100 (0.01%)

FIGURE 6

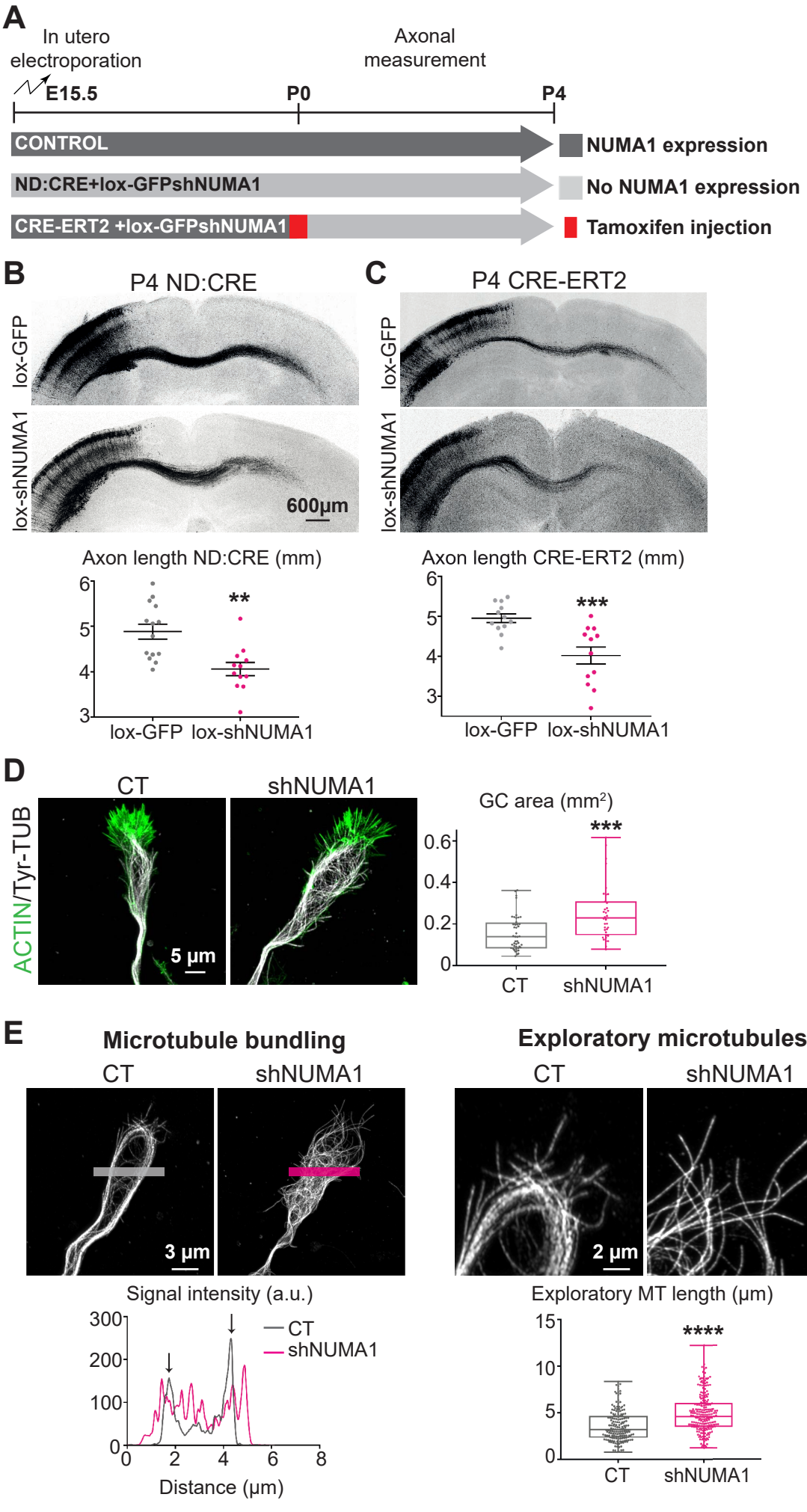
A
In utero electroporation
Axonal measurement
E15.5
P0
P4
CONTROL
NUMA1 expression
ND:CRE+lox-GFPshNUMA1
No NUMA1 expression
CRE-ERT2 +lox-GFPshNUMA1
Tamoxifen injection
B
P4 ND:CRE
lox-GFP
lox-shNUMA1
600µm
Axon length ND:CRE (mm)
**
lox-GFP
lox-shNUMA1
C
P4 CRE-ERT2
lox-GFP
lox-shNUMA1
Axon length CRE-ERT2 (mm)
***
lox-GFP
lox-shNUMA1
D
CT
shNUMA1
ACTIN/Tyr-TUB
5 µm
GC area (mm²)
***
CT
shNUMA1
E
Microtubule bundling
CT
shNUMA1
3 µm
Signal intensity (a.u.)
CT
shNUMA1
Distance (µm)
Exploratory microtubules
CT
shNUMA1
2 µm
Exploratory MT length (µm)
****
CT
shNUMA1

FIGURE 7

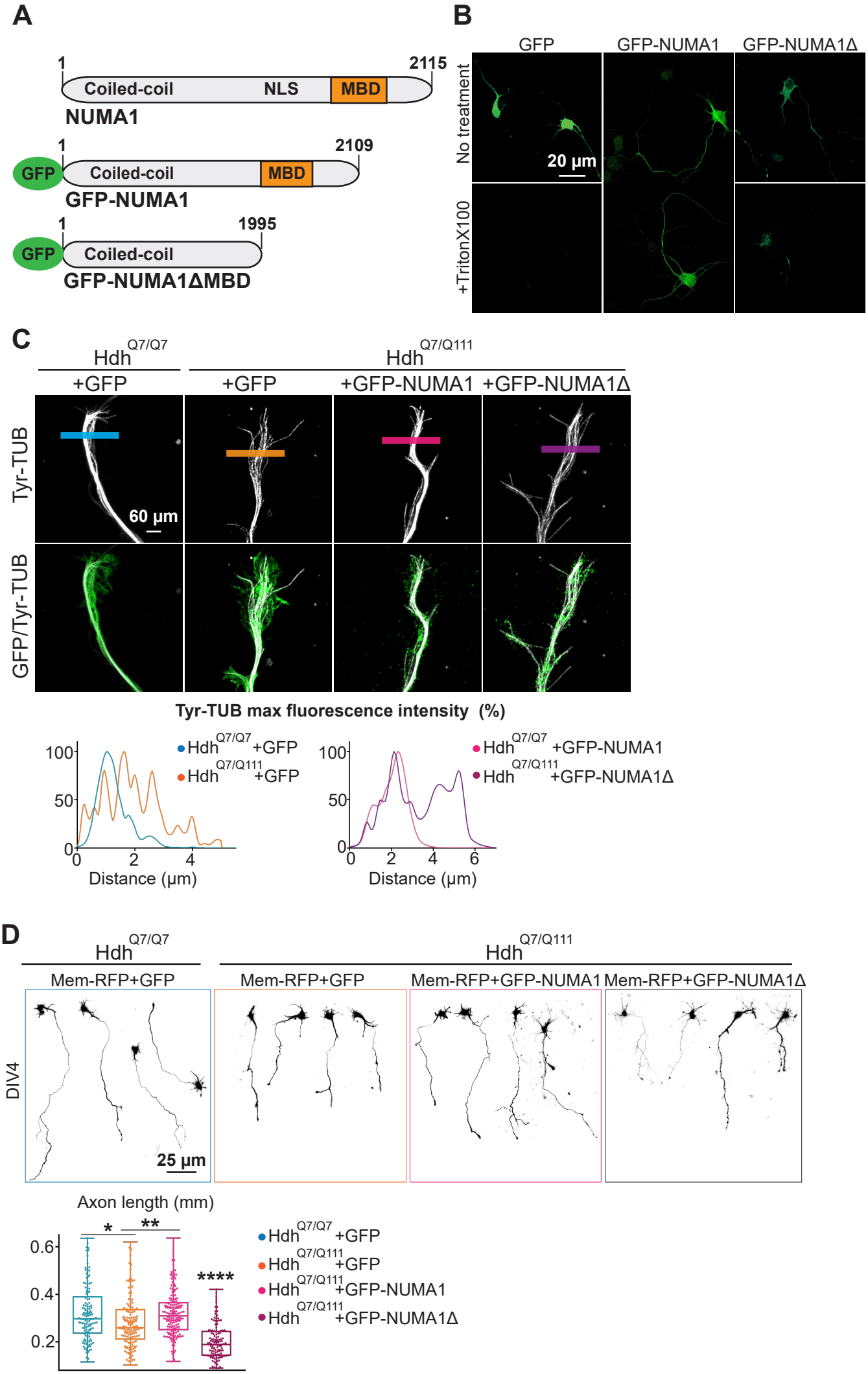
A
1
2115
Coiled-coil
NLS
MBD
NUMA1
1
2109
GFP
Coiled-coil
MBD
GFP-NUMA1
1
1995
GFP
Coiled-coil
GFP-NUMA1ΔMBD
B
GFP
GFP-NUMA1
GFP-NUMA1Δ
No treatment
+TritonX100
20 µm
C
Hdh Q7/Q7
Hdh Q7/Q111
+GFP
+GFP
+GFP-NUMA1
+GFP-NUMA1Δ
Tyr-TUB
GFP/Tyr-TUB
60 µm
Tyr-TUB max fluorescence intensity (%)
Hdh Q7/Q7 +GFP
Hdh Q7/Q111 +GFP
Hdh Q7/Q7 +GFP-NUMA1
Hdh Q7/Q111 +GFP-NUMA1Δ
Distance (µm)
Distance (µm)
D
Hdh Q7/Q7
Hdh Q7/Q111
Mem-RFP+GFP
Mem-RFP+GFP
Mem-RFP+GFP-NUMA1
Mem-RFP+GFP-NUMA1Δ
DIV4
25 µm
Axon length (mm)
*
**
****
Hdh Q7/Q7 +GFP
Hdh Q7/Q111 +GFP
Hdh Q7/Q111 +GFP-NUMA1
Hdh Q7/Q111 +GFP-NUMA1Δ

FIGURE 8

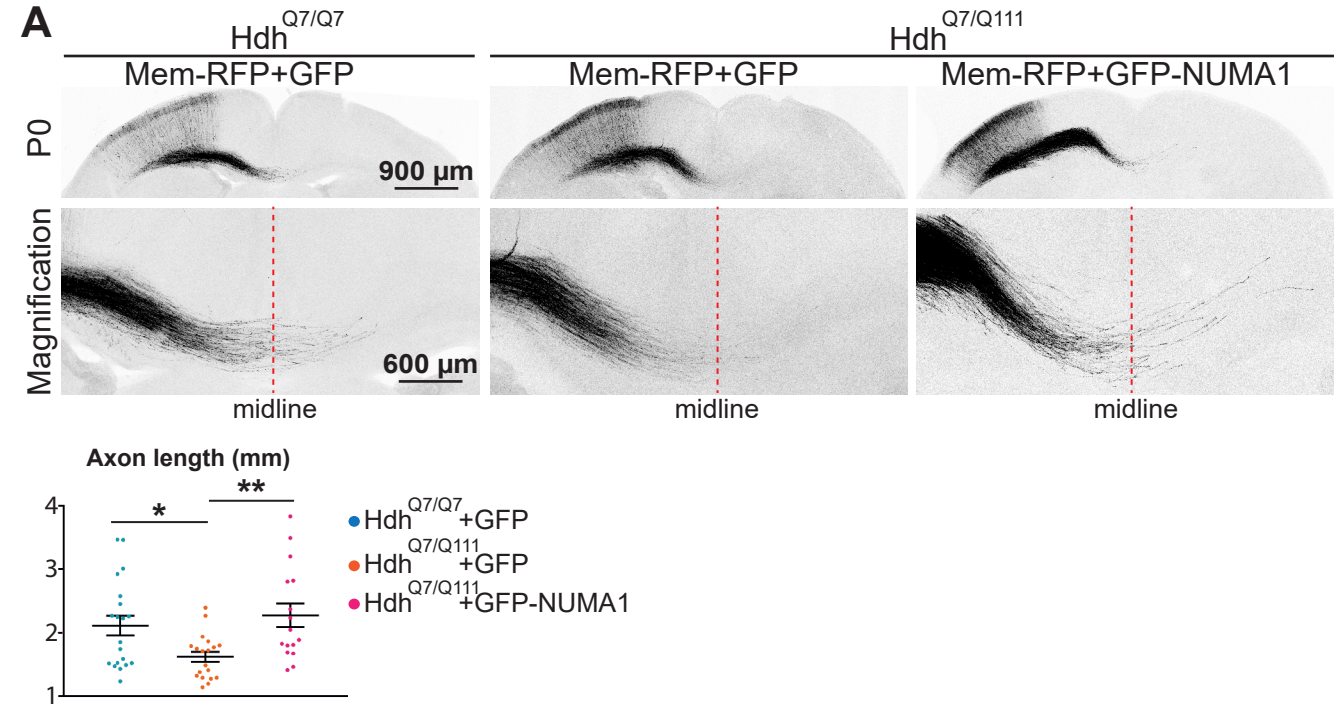
A
Hdh Q7/Q7
Hdh Q7/Q111
Mem-RFP+GFP
Mem-RFP+GFP
Mem-RFP+GFP-NUMA1
P0
900 µm
Magnification
600 µm
midline
midline
midline
Axon length (mm)
*
**
4
3
2
1
Hdh Q7/Q7 +GFP
Hdh Q7/Q111 +GFP
Hdh Q7/Q111 +GFP-NUMA1

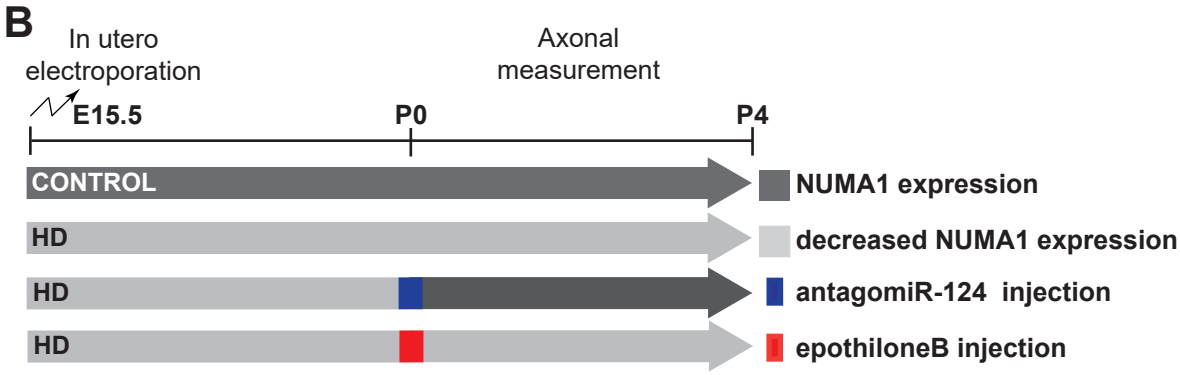
B
In utero electroporation
Axonal measurement
E15.5
P0
P4
CONTROL
HD
HD
HD
NUMA1 expression
decreased NUMA1 expression
antagomiR-124 injection
epothiloneB injection

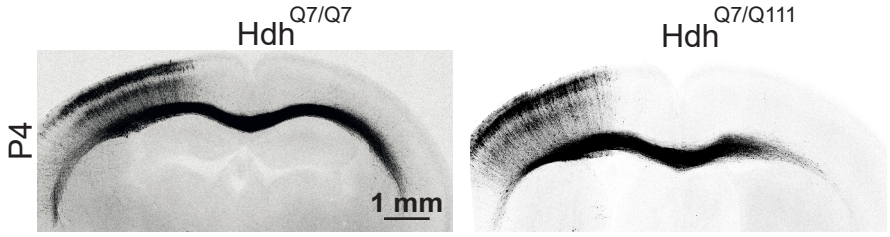
Hdh Q7/Q7
Hdh Q7/Q111
P4
1 mm

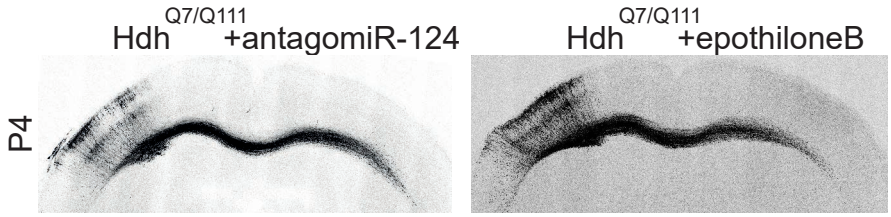
Hdh Q7/Q111 +antagomiR-124
Hdh Q7/Q111 +epothiloneB
P4

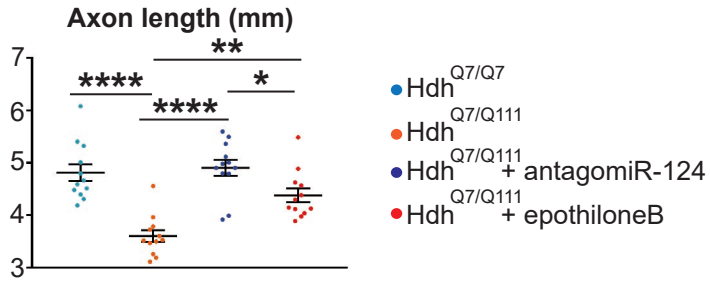
Axon length (mm)
**
****
*
****
7
6
5
4
3
Hdh Q7/Q7
Hdh Q7/Q111
Hdh Q7/Q111 + antagomiR-124
Hdh Q7/Q111 + epothiloneB

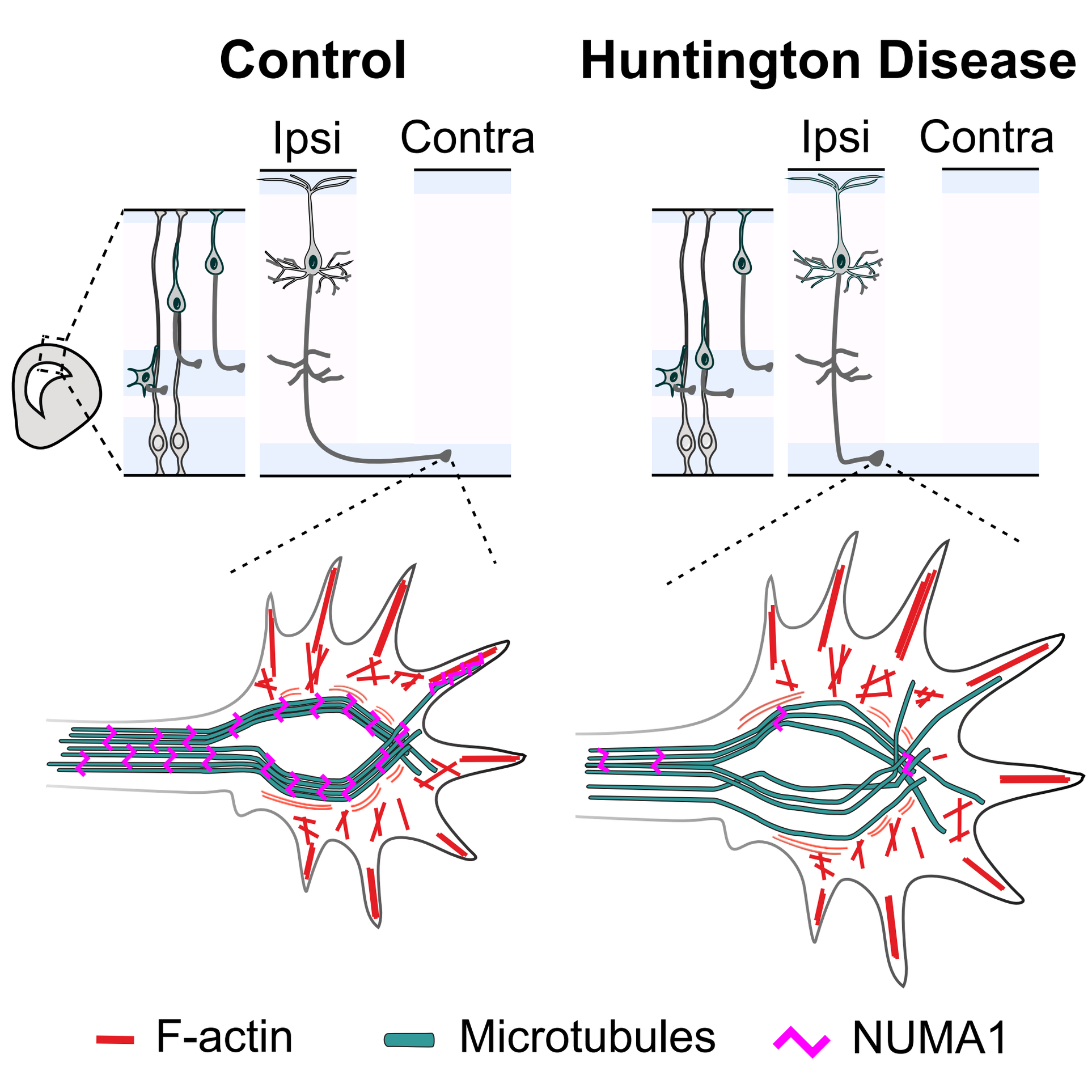
Control
Huntington Disease
Ipsi
Contra
Ipsi
Contra
F-actin
Microtubules
NUMA1